Short-term molecular consequences of chromosome mis-segregation for genome stability

Lorenza Garribba[1,#], Giuseppina De Feudis[1,#], Valentino Martis[1], Martina Galli[2], Marie Dumont[3], Yonatan Eliezer[4], René Wardenaar[5], Marica Rosaria Ippolito[1], Divya R Iyer[6], Andréa E Tijhuis[5], Diana CJ Spierings[5], Michael Schubert[5], Silvia Taglietti[1], Chiara Soriani[1], Simon Gemble[3], Renata Basto[3], Nick Rhind[6], Floris Foijer[5], Uri Ben-David[4], Daniele Fachinetti[3], Ylli Doksani[2] and Stefano Santaguida[1,7,8,*]

1. Department of Experimental Oncology at IEO, European Institute of Oncology IRCCS, Via Adamello 16, 20139 Milan, Italy

2. IFOM ETS - The AIRC Institute of Molecular Oncology, via Adamello 16, 20139, Milan, Italy

3. Institut Curie, PSL Research University, CNRS, UMR144, Paris, France

4. Department of Human Molecular Genetics and Biochemistry, Faculty of Medicine, Tel Aviv University, Tel Aviv, Israel

5. European Research Institute for the Biology of Ageing, University of Groningen, University Medical Center Groningen, 9713 AV, Groningen, the Netherlands

6. Department of Biochemistry and Molecular Biotechnology, University of Massachusetts Chan Medical School, 364 Plantation Street, Worcester, MA 01605, USA

7. Department of Oncology and Hemato-Oncology, University of Milan, Via Santa Sofia 9/1, 20122 Milan, Italy

8. Lead Contact

#These authors contributed equally

*Correspondence: stefano.santaguida@ieo.it (SS)

Keywords: aneuploidy, cancer, genome instability, MiDAS, asymmetric DNA damage segregation, senescence, mitotic errors, chromosomal instability

Abstract

Chromosome instability (CIN) is the most common form of genome instability and is a hallmark of cancer. CIN invariably leads to aneuploidy, a state of karyotype imbalance. Here, we show that aneuploidy can also trigger CIN. We found that aneuploid cells experience DNA replication stress in their first S-phase and precipitate in a state of continuous CIN. This generates a repertoire of genetically diverse cells that can either continue proliferating or stop dividing. Cycling aneuploid cells display lower karyotype complexity compared to the arrested ones and increased expression of DNA repair signatures. Interestingly, the same signatures were upregulated in highly-proliferative cancer cells, which might enable them to proliferate despite the disadvantage conferred by aneuploidy-induced CIN. Altogether, our study reveals the short-term origins of CIN following aneuploidy and indicates the aneuploid state of cancer cells as a point mutation-independent source of genome instability, providing an explanation for aneuploidy occurrence in tumors.

Introduction

Chromosomal instability (CIN), a condition of continuous chromosome mis-segregation, is a pervasive feature of tumors[1,2]. CIN confers enhanced evolutionary capabilities on cancer cells by increasing intratumor heterogeneity and by enabling chemoresistance[3–6]. CIN leads invariably to aneuploidy, a state of karyotype imbalances, found in more than 90% of solid tumors and about 65% of blood cancers[1]. The presence of aneuploid karyotypes leads to several detrimental defects, including proteotoxic stress[7–9], metabolic alterations[10] and induction of DNA damage[7,11–14].

Importantly, karyotype aberrations strongly correlate with poor patient prognosis[2]. This might be due to the fact that specific aneuploidies could confer a proliferative advantage, thus fueling tumorigenesis[5,6] and promoting survival under sub-optimal conditions[3,4]. Such an advantage could be explained by the possibility that aneuploidy induces CIN (and, more broadly, genome instability), which might enable a continuous sculpting of the genome, eventually leading to cumulative haploinsufficiency and triplosensitivity[15,16] of genes crucial for sustained proliferation. In agreement with this idea, studies in yeast have demonstrated that gain of a single chromosome leads to defective DNA damage repair[12]. Further, aneuploid strains often divide in presence of unrepaired DNA, which triggers chromosomal translocations[17]. Similar observations were made in higher eukaryotes[18]. For example, a comparison between trisomic and diploid human cells has revealed that aneuploid cells are characterized by increased frequency of lagging chromosomes in anaphase. Thus, this evidence points at aneuploidy as an instigator of genome instability[16]. It is plausible that this instability is due to the strong impact of karyotype abnormalities on gene expression and protein homeostasis. In fact, aneuploid cells were found to display imbalances in factors critical for DNA replication (such as

62 MCM2-7), DNA repair and mitosis[13], processes that are all fundamental for the maintenance of
63 genome integrity. In line with this possibility, previous studies have revealed that aneuploid cells
64 exhibit an increased S-phase duration, display reduced DNA replication fork rate and increased fork
65 stalling[13,14]. Due to the intrinsic genomic instability and other stresses typically associated with
66 aneuploidy, cells with abnormal karyotypes often exhibit delayed cell cycle progression. In some
67 cases, they even lose their proliferative capacity and stop dividing[1,14,19], resulting in their reduced
68 sensitivity to chemotherapies[20,21].
69 Given the high prevalence of unbalanced karyotypes in tumors and its impact on the proliferation of
70 cancer cells[3–6], elucidating the contribution of aneuploidy to genome instability, deciphering the
71 molecular mechanisms by which it occurs and deconvolving its cellular consequences remain of
72 paramount importance in cancer biology.
73 Here, by inducing controlled chromosome mis-segregation in otherwise pseudo-diploid human cells,
74 we set out to identify the origins of genome instability in aneuploid cells and to understand whether
75 protective mechanisms operate to preserve genome integrity. Our data indicate that in the first S-
76 phase following chromosome mis-segregation, aneuploid cells fire dormant replication origins
77 through a DDK-dependent mechanism and complete replication of genomic loci through mitotic
78 DNA synthesis (MiDAS). Importantly, those pathways, acting both in interphase and mitosis, are
79 crucial for aneuploid cells to protect them against further genome instability. We also show that the
80 DNA damage associated with aneuploidy can be distributed asymmetrically between daughter cells
81 during cell division and this, at least partially, can explain why some cells (*i.e.* those who have
82 inherited most of the damage) stop dividing. By establishing a method for the separation of arrested
83 and cycling aneuploid cells, we found that cycling aneuploid cells exhibit increased expression of
84 DNA repair genes. Interestingly, the same transcriptional signature was upregulated in cancer cells
85 characterized by high proliferative capacity. We speculate that elevated expression of DNA damage
86 repair genes in highly proliferative cancers is able to help them counteracting the burden associated
87 with genome instability, allowing them to benefit from a continuous reshuffling of the karyotype,
88 which is crucial to sustain enhanced proliferation[3,4]. Finally, we speculate that interfering with those
89 pathways, including DDK-mediated origin firing and MiDAS, is crucial for limiting DNA damage
90 and might provide novel therapeutic interventions in cancer therapy. An example of this is given by
91 ongoing clinical trials involving agents inhibiting DDK-mediated origin firing (*e.g.*,
92 ClinicalTrials.gov Identifier: NCT03096054 and NCT05028218), and our work might help in the
93 stratification of patients who could benefit from those treatments based on their proliferative capacity.
94

95 **Results**

96 **Identification of mechanisms responsible for tolerance to aneuploidy-induced replication stress**
97 Aneuploidy is associated with increasing genome instability[16], affecting the fidelity of both genome
98 replication and segregation. To dissect the mechanisms through which aneuploid cells seek to limit
99 this instability and thus keep proliferating, we quantified the direct effects of aneuploidy on genome
100 integrity. For this, we analyzed chromosome aberrations immediately after the induction of mitotic
101 errors (1st mitosis) and after one cell cycle (2nd mitosis). To this aim, we synchronized untransformed
102 and genomically-stable, pseudo-diploid hTERT RPE-1 cells with thymidine at the G1/S border
103 (Extended Data Fig. 1a,b) and, after release into the cell cycle, pulsed them with DMSO (vehicle
104 control) or reversine, an Mps1 inhibitor widely-used to generate aneuploid cells as a consequence of
105 chromosome segregation errors[22]. Cells were then either harvested for karyotype analysis of the 1st
106 mitosis or, after DMSO or reversine wash-out, allowed to continue in the cell cycle, and then
107 harvested for the same purpose in the 2nd mitosis (Fig. 1a). To rule out the possibility that the
108 synchronization method and/or reversine treatment would impact on DNA damage thus affecting the
109 results of our experiments, we evaluated the consequences of thymidine block and release in presence
110 of reversine using γH2AX as a marker of DNA damage (Extended Data Fig. 1c-e). We found that,
111 although thymidine block induced mild levels of DNA damage, this was fully repaired 12 hours after
112 washout with a similar kinetics in cells exposed to Mps1 inhibitor or vehicle control (Extended Data
113 Fig. 1c-e). We also treated cells with doxorubicin to induce DNA damage and observed no
114 statistically significant differences in the DNA repair capacity of cells treated with the Mps1 inhibitor
115 or vehicle control (Extended Data Fig. 1c,f,g). This shows that treatment with reversine does not
116 affect cell capacity to repair the damage. Thus, by using this approach, analysis of 1st mitosis provided
117 a measurement of the degree of chromosome aberrations directly caused by aneuploidy induction,
118 whereas quantification of 2nd mitosis allowed for the estimation of genome alteration as a
119 consequence of harboring aneuploid karyotypes. By using multi-color FISH (mFISH), we found
120 abnormal events – including gains, losses and translocations – in both the 1st and 2nd mitoses (Fig.
121 1b,c and Extended Data Fig. 1h,i). Importantly, the percentage of cells harboring more than 10
122 abnormal events more than tripled from the 1st to the 2nd mitosis (Fig. 1b,c) indicating that the
123 aneuploid state *per se* negatively impacts genome stability. However, we also note that Mps1i pulse
124 in the 1st mitosis could affect chromosome stability in a long-term and aneuploidy-independent
125 manner, through not-yet-identified mechanisms unrelated to chromosome mis-segregation.
126 Notably, numerical aneuploidies accounted for most of the measured aneuploidy events, both in the
127 1st and in the 2nd mitosis (Fig. 1d). Next, to decipher how aneuploidy affects genome integrity, we
128 examined at high resolution the 1st S-phase of newly-generated aneuploid cells. For this, we
129 synchronized cells at the G1/S border, released them in the presence of reversine or vehicle control,

130 blocked them in late G1 with mimosine and released them in S-phase (Fig. 1e and Extended Data
131 Fig. 2a,b). Similar to thymidine, mimosine leads to accumulation of mild levels of DNA damage that
132 is repaired over time no matter whether cells had received reversine or the vehicle control in the
133 previous 24 hours (Extended Data Fig. 2c-e). For the study of the 1st S-phase of aneuploid cells
134 obtained as above, we used three complementary approaches: 1) ultra-structural visualization of
135 replication forks through electron microscopy (EM), 2) single-cell analysis of replication stress and
136 DNA damage markers by immunofluorescence and 3) assessment of replication dynamics by DNA
137 combing (Fig. 1e). These efforts led to three key observations. First, EM analysis of replication
138 intermediates revealed an increase in reversed replication forks in aneuploid cells, compared to
139 pseudo-diploid counterparts (Fig. 1f,g). Accumulation of these intermediates is associated with an
140 increased frequency of replication fork stalling[23] and is consistent with previous observations of
141 ongoing replication stress in aneuploid cells[13,14]. Further, aneuploid cells displayed increased levels
142 of DNA replication stress and DNA damage markers such as FANCD2 (mean foci in control: 14,2 ±
143 1,9; aneuploid: 47,7 ± 4,6), RPA (mean foci in control: 8 ± 1,4; aneuploid 19,5 ± 2,7) and pChk1
144 (mean foci in control: 23 ± 1,8; aneuploid 33,3 ± 3,1) (Fig. 1h-m). Among them, the number of
145 FANCD2 foci per S-phase cell was found to be even higher in aneuploid cells than in cells treated
146 with the DNA replication inhibitor aphidicolin, used as a positive control (FANCD2 mean foci in
147 aphidicolin-treated cells: 40,7 ± 3; RPA mean foci 49 ± 3,9; pChk1 mean foci 44,1 ± 2,6) (Fig. 1i,k,m
148 and Extended Data Fig. 2f). Finally, we found that fork density and origin firing rate in aneuploid
149 cells were higher than euploid counterparts (Fig. 1n-p), suggesting that dormant replication origins
150 were fired in the 1st S-phase following chromosome mis-segregation events. In our previous study
151 we reported that aneuploid cells have reduced fork rate and a higher number of stalled forks as
152 compared to euploid cells[14]. Cells activate dormant origins in response to reduced fork rate and stalled
153 forks to ensure that the genome gets fully replicated in time. Hence, we estimated origin firing rate
154 and fork density, calculated as the total number of forks per Mb of DNA[24]. The total origin firing rate
155 was 2-fold higher in aneuploid cells compared to euploid cells ($p=1,5x10^{-34}$). Consistent with the
156 origin firing data, fork density was also 1,7-fold higher in aneuploid cells ($p=7,46x10^{-13}$). Analog-
157 specific estimations for both the parameters also showed similar trends. Our data is also consistent
158 with increased origin firing observed in aneuploid human pluripotent stem cells[25]. Overall, our data
159 shows that aneuploid cells struggle to complete replication and therefore activate backup mechanisms
160 such as dormant origin firing to ensure genome duplication and tolerance to replication stress.
161 Altogether, these data provide crucial insights into the effects of aneuploidy on genome integrity. We
162 find that: 1) cells harboring aneuploid karyotypes tend to accumulate increasing levels of
163 chromosome abnormalities, 2) those defects might be the consequence of DNA replication stress, and

164 3) are correlated with a higher incidence of replication fork reversal and increased DNA damage
165 markers. Finally, 4) at the same time, aneuploid cells also show an increased usage of dormant origins,
166 which we speculate might act as a mechanism to tolerate aneuploidy-induced replication stress.
167
168 **Aneuploid cells rely on DDK to cope with replication stress**
169 Dormant origin firing is a well-known rescue mechanism protecting cells during replication stress[26].
170 To test whether aneuploid cells would also rely on this salvage mechanism, we inhibited the activity
171 of DDK, a key player in origin firing[27–31]. For this, aneuploid cells or pseudo-diploid counterparts
172 (generated as in Fig. 1e) were arrested in late G1 (after the 1st mitosis) and then released in the
173 presence or absence of the DDK inhibitor XL413[32] (Fig. 2a). After 6 hours, cells were pulsed with
174 the thymidine analogue ethynyl deoxy-uridine (EdU) for 30 minutes to label S-phase cells and then
175 fixed and stained for FANCD2, RPA and pChk1. We found that inhibition of DDK led to significantly
176 increased levels of FANCD2 (mean foci in control: 40,9 ± 2,9; control + DDKi: 52,6 ± 2,9; aneuploid
177 72,2 ± 3,5; aneuploid + DDKi: 84,5 ± 4,9), RPA (mean foci in control: 56,3 ± 3,7; control + DDKi:
178 36,2 ± 2,9; aneuploid 83,5 ± 5,8; aneuploid + DDKi: 103,9 ± 6,4) and pChk1 (mean foci in control:
179 44,1 ± 2,6; control + DDKi: 44,9 ± 2,8; aneuploid 62,9 ± 4,2; aneuploid + DDKi: 74,7 ± 4,2) in
180 aneuploid cells, indicating that replication stress is exacerbated when interfering with dormant origin
181 firing through DDK inhibition (Fig. 2b-g). These findings were validated also by using alternative
182 approaches to interfere with the function of DDK and Mpsi, namely an analog-sensitive allele of
183 Cdc7[31] and the Mps1 inhibitor AZ3146[33], respectively (Extended Data Fig.3a). For this, we inhibited
184 Cdc7 using 20μM 1-NM-PP1 analog - a concentration previously shown[31] to fully inhibit Cdc7-
185 dependent phosphorylation of MCM2 (Extended Data Fig. 3b)- and induced aneuploidy using
186 AZ3146. We found that Cdc7 inhibition resulted in significantly increased levels of FANCD2, RPA
187 and pChk1 in aneuploid cells (Extended Data Fig. 3c-h), in agreement with experiments performed
188 with XL-413. We also observed a significant increase in the number of FANCD2 foci and a
189 significant decrease in that of RPA foci in control cells when Cdc7 was inhibited compared to
190 functional Cdc7 (Extended Data Fig. 3c,d), which highlights the importance of DDK activity during
191 replication stress and is in agreement with previous findings[31]. These results prompted us to test
192 whether DDK activity, and its involvement in dormant origin firing, would also be critical for
193 aneuploid cell proliferation. Interestingly, we found that aneuploid cells were more sensitive to DDK
194 inhibition compared to pseudo-diploid counterparts (Fig. 2h,i) - although showing a similar rate of
195 cell death under basal conditions (Extended Data Fig. 3i)-, indicating that they rely more than euploid
196 cells on the function of DDK to survive. Altogether, our data show that DDK-mediated origin firing
197 represents a protective mechanism that acts in S-phase of aneuploid cells to limit replication stress.

198 Importantly, inhibition of this mechanism exacerbates replication stress in aneuploid cells and
199 reduces their viability.
200
201 **Aneuploid cells undergo mitotic DNA synthesis to limit the consequences of replication stress**
202 **on genome stability**
203 DNA replication stress - defined as any slowing or stalling of replication fork progression and/or
204 DNA synthesis[34]- impacts mitotic fidelity[35–37]. Thus, we thought to study how the events occurring
205 in the 1st S-phase of aneuploid cells affect the following cell division. To this aim, we performed live-
206 cell imaging experiments with hTERT RPE-1 cells stably expressing PCNA-GFP and H2b-RFP. This
207 allowed to monitor S-phase length through the measurement of time elapsed between appearance and
208 disappearance of PCNA foci (a well-known feature of this DNA clamping factor[38]) and mitotic timing
209 and quality by tracking chromosomes through H2b. Cells were synchronized with thymidine, then
210 pulsed with reversine while they were transiting through the 1st mitosis. Cells were then washed-out
211 and imaged every 10 minutes for 72 hours in order to evaluate the duration of the first S-phase after
212 chromosome mis-segregation and the quality of the 2nd mitosis (Fig. 3a,b). First, we found that
213 aneuploid cells displayed a longer S-phase compared to euploid controls (mean S-phase length in
214 control: 540,1 ± 17,82; aneuploid: 662,5 ± 29,89. Extended Data Fig. 4a), in agreement with the fact
215 that they experience ongoing DNA replication stress and in line with previous reports[13,14]. Next, we
216 decided to correlate S-phase length to the quality of the 2nd mitosis. Thus, we classified mitotic figures
217 in "normal mitoses", for those not displaying defects, and "abnormal mitoses", for those showing
218 mitotic errors, including chromatin bridges, lagging chromosomes or micronuclei in the following
219 G1. Interestingly, we found a positive correlation between S-phase length and frequency of abnormal
220 mitoses (mean S-phase length in control: 603,3 ± 55,4; aneuploid: 728,7 ± 46,2) (Fig. 3c). Further,
221 aneuploid cells that displayed mitotic errors spent more time in mitosis (Fig. 3d), which we could
222 fully attribute to spindle-assembly checkpoint activation, since SAC inhibition rescued this delay
223 (Extended Data Fig. 4b).
224 Based on the evidence that aneuploid cells suffer from replication stress in the 1st S-phase following
225 chromosome mis-segregation events, we wanted to investigate whether they would attempt to finish
226 DNA replication in the subsequent mitosis, as previously discovered in cancer cells as a consequence
227 of S-phase stress[39]. In order to evaluate the activation of the mitotic DNA synthesis (MiDAS)
228 pathway, aneuploid cells generated as in Fig. 1a were arrested at the G2/M boundary with the CDK1
229 inhibitor RO3306 (Extended Data Fig. 4c,d – a synchronization method that did not induce DNA
230 damage accumulation (Extended Data Fig. 4e-g)) and released in the presence of EdU and colcemid
231 to monitor sites of active DNA synthesis in prometaphase cells. By doing so, we observed that the

232 number of EdU foci per spread was significantly higher in aneuploid cells in comparison to the control
233 (mean EdU foci in control: 0,1 ± 0,04; aneuploid: 0,9 ± 0,1; Fig. 3e,f). The DNA replication inhibitor
234 aphidicolin was added in S-phase as replication stress inducer (mean EdU foci: 2,6 ± 0,3).
235 Interestingly, we did not spot a tendency of MiDAS to occur at defined chromosomal locations such
236 as telomeres, similarly to aphidicolin-induced MiDAS (Extended Data Fig. 4h,i). Next, to test the
237 efficacy of MiDAS in fixing unfinished DNA replication, we inhibited the pathway and evaluated the
238 consequences on genome stability in the following G1 (Fig. 3g). To this aim, we first tested if MiDAS
239 could be inhibited by adding a high dose of aphidicolin in mitosis similarly as observed in cancer
240 cells[39–41]. Our results showed that indeed this was the case, since the number of EdU foci per
241 prometaphase cell was significantly reduced upon addition of aphidicolin in mitosis (mean EdU foci
242 in control: 0,2 ± 0,1; control + MiDASi: 0,1 ± 0,03; aneuploid: 1,3 ± 0,2; aneuploid + MiDASi: 0,5
243 ± 0,1; Fig. 3h,i). As readouts of genome instability, we analyzed 53BP1 bodies and micronuclei in
244 the G1 after the 2nd mitosis in which MiDAS had occurred. We found that both 53BP1 bodies per cell
245 and the frequency of G1 cells with micronuclei were significantly increased in aneuploid cells in
246 which MiDAS was inhibited in comparison with those in which MiDAS occurred properly (Fig. 3j-
247 l). This correlation was also observed in aphidicolin-treated cells (mean EdU foci: 4,5 ± 0,6; +
248 MiDASi: 0,7 ± 0,3), in agreement with previous studies[39]. These findings were further confirmed by
249 depleting the non-catalytic subunit of DNA polymerase δ POLD3, which has been shown to be
250 essential for the two MiDAS pathways described so far[39,41]. By using this approach and employing
251 AZ3146 to induce aneuploidy (Extended Data Fig. 5a,b), we found that POLD3 depletion inhibited
252 MiDAS (Extended Data Fig. 5c,d) and prevented the accumulation of 53BP1 bodies and micronuclei
253 in aneuploid cells (Extended Data Fig. 5e-g). Altogether, our data demonstrate that MiDAS acts as a
254 safeguard mechanism in the 2nd mitosis to prevent genome instability from further increasing.
255

256 **Dormant origin firing and MiDAS protect aneuploid cells from further increase in genome**
257 **instability**

258 The results obtained from the characterization of the first S-phase after chromosome mis-segregation
259 and the subsequent mitosis revealed two protective mechanisms operating in aneuploid cells with the
260 role of limiting genome instability. To test if the combined action of these two pathways indeed serves
261 to protect aneuploid cells, we simultaneously inhibited DDK in S-phase and MiDAS in the
262 subsequent M phase and evaluated DNA damage and chromosomal aberrations in the following G1
263 phase (Fig. 4a). As DNA damage markers, we used FANCD2, a reliable replication stress/DNA
264 damage marker in aneuploid cells (Fig. 1i and Extended Data Fig. 3c,d), and γH2AX, an early marker
265 of DNA double-stranded breaks[42]. To specifically look at G1 cells, we used cytochalasin B to block

266 cytokinesis and analyze daughter cells[43]. We observed that the number of both FANCD2 and γH2AX
267 foci was significantly higher in aneuploid cells in which DDK and MiDAS were inhibited compared
268 to aneuploid cells in which only either DDK or MiDAS was hindered (Fig. 4b-d). Interestingly,
269 inhibition of both pathways led to an increase in FANCD2 and γH2AX foci also in euploid cells,
270 highlighting that their proper functioning is crucial for maintaining genome integrity. Then, to assess
271 the frequency of chromosomal aberrations upon DDK and MiDAS inhibition, G1 cells were treated
272 with the PP1/PP2A phosphatase inhibitor calyculin A to induce premature DNA condensation[44] and
273 obtain metaphase-like spreads. By mFISH analysis, we were able to observe an almost 2-fold increase
274 in the percentage of cells with translocations between aneuploid cells in which DDK and MiDAS
275 were or were not inhibited (mean percentage of cells with at least 1 translocation in aneuploid cells:
276 33,4; in aneuploid cells + DDKi + MiDASi: 63,2) (Fig. 4e-g). Taken together, these data indicate that
277 the presence of both pathways protects aneuploid cells from further increasing their genome
278 instability.
279 Interestingly, while scoring DNA damage in G1 cells we noticed that distribution of FANCD2 or
280 γH2AX foci in aneuploid cells was not always symmetric between daughter cells. Thus, we
281 specifically analyzed the pattern of DNA damage inheritance in the aneuploid sample and the euploid
282 control, along with aphidicolin-treated cells where it has been recently shown that DNA damage can
283 be distributed asymmetrically between daughters[45]. Our data indicated that FANCD2 and γH2AX
284 foci were asymmetrically distributed in about 20% and 10% of aneuploid daughter cells, respectively
285 (Fig. 4h-j). We then decided to follow the fate of aneuploid daughter cells via live cell imaging and
286 asked whether asymmetric DNA damage distribution would impinge on proliferative capacity. For
287 this, we used hTERT RPE-1 cells expressing H2b-GFP and RNF168-miRFP - as a marker of DNA
288 damage- and assessed DNA damage inheritance in aneuploid cells over a 5-day timeframe (Extended
289 Data Fig. 6a). First, in agreement with our findings obtained by monitoring FANCD2 and γH2AX in
290 fixed cells, we found RNF168 to be asymmetrically partitioned in more than 20% of daughter cells
291 (Extended Data Fig. 6b-d). Second, DNA damage transmission from mother to daughter cells was
292 more likely to happen in aneuploid cells eventually displaying impaired proliferative capacity
293 (defined as those cells that divided less than 4 times over a 5-day period (see Methods) - Extended
294 Data Fig. 6e), pointing at a correlation between DNA damage accumulation and reduced proliferative
295 capacity. Lastly, and most importantly, the incidence of cell divisions in which DNA damage was
296 asymmetrically distributed between daughter cells was higher in cells with low proliferative capacity
297 (Extended Data Fig. 6f), indicating that unequal partitioning of DNA damage may act as an
298 accelerator of cell cycle arrest in aneuploid cells. These data suggest that non-random distribution of
299 DNA damage between aneuploid daughter cells, alone or in combination with other aneuploidy-

300 associated features, such as micronucleation, proteotoxic stress, etc., could underlie the difference in
301 proliferation observed among aneuploid cells[14,19].
302
303 **A method to separate arrested and cycling aneuploid cells**
304 The asymmetric inheritance of DNA damage and cell fate determinants have been hypothesized to
305 underlie stem cell self-renewal[46]. Thus, based on asymmetric portioning of DNA damage markers in
306 aneuploid cells (Fig. 4h-j and Extended Data Fig. 6), we reasoned that, like stem cells, they might
307 segregate DNA damage asymmetrically, partially explaining why some aneuploid cells can keep
308 cycling while others get arrested and enter senescence[14,19]. To test this hypothesis, we first needed to
309 confirm that a proportion of aneuploid cells indeed gets arrested in the cell cycle and becomes
310 senescent over time. Hence, we let aneuploid cells progress for about 3 cell cycles before harvesting
311 them for β-galactosidase staining, a widely used marker of senescence[47]. As a positive control, we
312 used cells treated with doxorubicin for 7 days, as DNA damage is an established senescence-
313 inducer[14]. Our results indicated that, as expected[14], there was a sub-population of senescent cells in
314 the aneuploid sample (Fig. 5a). Also, by conducting the same experiment at earlier time points (*i.e.*,
315 1, 2 or 3 cell cycles after aneuploidy induction), we found there was an accrual of senescent cells over
316 time with a peak at 72 hours after chromosome mis-segregation, reflecting the increase in genome
317 instability as an important trigger of senescence in aneuploid cells (Extended Data Fig. 7a). To
318 characterize, in detail, the aneuploid cells that were still able to cycle and those that underwent
319 senescence, we decided to establish a method for their isolation and separation. For this, we reasoned
320 that the main (and, at the same time, potentially exploitable) difference between aneuploid cycling
321 and arrested cells is that the latter are senescent. Thus, we adapted to aneuploid cells a FACS sorting-
322 based assay employing the fluorescent substrate of the β-galactosidase enzyme (which is highly active
323 in senescent cells) 9H-(1,3-dichloro-9,9-dimethylacridin-2-one-7-yl) β-d-galactopyranoside
324 (DDAOG)[48]. We then exposed aneuploid cells to DDAOG and separated cells that were able to
325 metabolize it (*i.e.*, senescent cells) from those that could not metabolize it (*i.e.*, cycling cells) (Fig.
326 5b,c and Extended Data Fig. 7b,c). First, we confirmed that sorted cells were indeed either arrested
327 or cycling by β-galactosidase staining and found the former to be highly reactive to senescence-
328 associated β-galactosidase staining (Fig. 5d). Further, we used hTERT FUCCI RPE-1 cells[49]
329 (Extended Data Fig. 7d) to obtain the cell cycle profile of the two sorted aneuploid cell populations,
330 together with the aneuploid sample before sorting and the euploid control. Our data confirmed that
331 aneuploid cells positive for DDAOG were indeed arrested, since the vast majority of them (86 ±
332 14,1%) were stuck in G1, as expected for senescent cells. On the other hand, negative ones were able
333 to proliferate (Extended Data Fig. 7e and Fig. 5e,f) and the percentage of G1 cells was 24% (± 8,5%)

334 (Extended Data Fig. 7e and Fig. 5e,f). Collectively, these data indicate that our method allows for the
335 successful separation and recovery of arrested and cycling aneuploid cells that could be used for
336 further analysis and characterization of the two populations.
337
338 **DNA damage and karyotype complexity might be responsible, at least partially, for cell cycle**
339 **defects of aneuploid cells**
340 We then evaluated DNA damage in cycling and arrested aneuploid cells, as well as in aneuploid cells
341 before sorting and the euploid control. Our data indicate that aneuploid arrested cells display
342 increased levels of FANCD2 and γH2AX foci compared to aneuploid cycling cells (mean FANCD2
343 foci in aneuploid arrested: 71,8 ± 3,9; in aneuploid cycling: 46,9 ± 2,2; mean γH2AX foci in aneuploid
344 arrested: 6,4 ± 1,1; in aneuploid cycling 2,5 ± 0,5) (Fig. 5g-i). Further, we also analyzed the karyotype
345 of cycling and arrested aneuploid cells by single-cell whole genome sequencing (scWGS) and
346 observed an increased frequency of cells with at least 3 aneuploid chromosomes in arrested aneuploid
347 cells (Fig. 5j,k) without showing any clear trend of specific gained/lost chromosomes (Extended Data
348 Fig. 7f,g). Altogether, these data show that both DNA damage and severe karyotype imbalances might
349 contribute, at least partially, to cell cycle arrest in aneuploid cells.
350
351 **Cycling aneuploid cells display increased expression of DNA repair genes**
352 In line with reduced DNA damage and karyotype abnormalities in the aneuploid cells that retained
353 their proliferation capacity, we found that the frequency of mitotic errors (such as anaphase bridges
354 and micronuclei) in aneuploid cycling cells was comparable to that of controls for at least 3
355 generations (Fig. 6a-c). This result suggests that the karyotype of these cells is likely to remain stable
356 over time, which is indicative of low levels of genome instability in aneuploid cycling cells. Having
357 established a tool to separate the two sub-populations of aneuploid cells, we turned our attention to
358 the identification of features distinguishing aneuploid cycling cells from those that arrested. To
359 address this question, we decided to analyze their transcriptional signatures via RNAseq. This
360 analysis revealed that the two samples are indeed quite different (Fig. 6d). In particular, aneuploid
361 arrested cells displayed overexpression of p53 and inflammation-related genes, in agreement with
362 previous findings[14]. Conversely, aneuploid cycling cells, as expected based on their retained ability
363 to divide, exhibited increased expression of cell cycle genes compared to aneuploid arrested cells.
364 Interestingly, we also noticed that DNA damage and repair genes were overexpressed in aneuploid
365 cycling cells (Fig. 6d and Extended Data Table 1). Consistently, pathways associated with DNA
366 damage repair were up-regulated in cycling *vs* arrested aneuploid cells (Fig. 6e). In line with this,
367 when exposed to ionizing radiation (IR), cycling aneuploid cells were able to repair DNA damage

368 more efficiently than the arrested ones (Fig. 6f,g and Extended Data Fig. 8a,b). Indeed, we measured
369 a faster decay kinetics of γH2AX and 53BP1 levels in the cycling population compared to the arrested
370 one (Fig. 6f,g and Extended Data Fig. 8a,b), that holds true for γH2AX also when compared to euploid
371 controls (Extended Data Fig. 8c,d). Non-sorted aneuploid cells were also included in the analysis,
372 and they turned out to have a lower efficiency compared to the euploid controls in fixing IR-induced
373 DNA damage (Extended Data Fig. 8a,b,e,f). Increased expression of DNA damage repair genes found
374 in aneuploid cycling cells could be due to their higher proliferative capacity compared to the arrested
375 ones or the presence of euploid cells in the population (which were ~1.8-fold more in cycling
376 aneuploid cells compared to the arrested ones (24% *vs.* 13%, respectively) - Fig. 5j,k). To determine
377 whether cycling aneuploid cells indeed upregulate DDR pathways, we compared their transcriptome
378 to that of (cycling) euploid counterparts. As expected, when compared to euploid, cycling aneuploid
379 cells downregulate pathways associated with cell proliferation and upregulate the p53 pathway
380 (Extended Data Fig. 8g). Nonetheless, we found DNA repair gene expression to be higher in
381 aneuploid cycling cells even when compared to euploid control cells (Extended Data Fig. 8h). As
382 cycling aneuploid cells upregulate the DDR both in comparison to euploid cells and to arrested
383 aneuploid cells, we conclude that this is not a consequence of higher proliferative capability and/or
384 driven by a small fraction of diploid cells present in the population. Importantly, the activation of
385 DNA damage repair pathways in aneuploid cells is consistent with our recent findings in cancer[20] and
386 untransformed cells[50]. We therefore hypothesized that higher expression of DNA damage repair
387 genes would confer a growth advantage to the cells. To confirm this, we turned to the CCLE (Cancer
388 Cell Line Encyclopedia) database[51,52] to analyze the association between doubling time and DNA
389 damage repair gene expression in more than 400 human cancer cell lines. We divided the cell lines
390 into top and bottom quartiles based on their doubling times, and then compared their gene expression
391 profiles. Cell lines with a low doubling time (<35 hours) exhibited increased expression of DNA
392 repair related gene signatures in comparison to cells with a high doubling time (>65 hours) (Fig. 6h-
393 j), linking high levels of DDR with increased proliferation capacity. These data suggest that elevated
394 expression of DDR genes might confer a proliferative advantage to aneuploid cells and make them
395 able to cycle despite the disadvantage conferred by the aneuploid status. Altogether, our data reveal
396 the existence of protective mechanisms in aneuploid cells, namely DDK-mediated origin firing in S-
397 phase and MiDAS in the subsequent mitosis, which operate to limit their genome instability (Fig. 7).
398 Also, increasing degrees of karyotype aberrations together with high levels of DNA damage could
399 contribute, at least partially, to cell cycle arrest of aneuploid cells. Lastly, an increased capacity to
400 repair DNA damage is associated with a proliferative advantage not only in untransformed but also
401 in cancer cells (Fig. 7).

402

403 ## Discussion

404 Genome instability is a hallmark of cancer[53]. Its most common form is CIN, shown to promote
405 tumorigenesis and confer proliferative advantages to cancer cells[3–6]. CIN can directly cause
406 aneuploidy and, in this study, we demonstrate that aneuploidy can also instigate CIN. By combining
407 biochemical and live cell imaging experiments with single-molecule replication-mapping
408 technologies and single-cell multi-omics analysis, we found that the acquisition of unbalanced
409 karyotypes can directly contribute to short-term genome instability, which in turn yields a diverse
410 array of karyotypic landscapes. This effect feeds a self-sustaining loop, in which aneuploidy leads to
411 CIN, thus generating more aneuploid daughter cells able to propagate genome diversity through
412 continuous errors during genome replication and segregation.

413 Previous reports have shown that aneuploid cells can experience replication stress[13,14]. Here, we show
414 that a DDK-dependent dormant origin firing operates during the first S-phase following chromosome
415 mis-segregation and acts as a protective mechanism to cope with replication stress. It is still unclear
416 what are the actual sources of replication stress in aneuploid cells. DNA replication stress can be
417 triggered by 1. collisions between the replication fork and the transcriptional machinery, 2. nucleotide
418 pool imbalances, 3. difficulties in the template DNA (*e.g.*, repetitive sequences and/or secondary
419 structures), 4. scarcity of replication factors to perform DNA synthesis[34]. Among them, insufficient
420 amount of replication factors seems to be the most likely cause of replication stress in aneuploid cells,
421 based on the fact that decreased levels of MCM2-7 proteins were reported in RPE-1 and HCT116
422 stable aneuploid clones with defined trisomies[13]. Also, a recent study has revealed that tetraploid cells
423 encounter replication stress as a result of insufficiency of DNA replication factors[54], a mechanism
424 that could also apply to aneuploid cells. Because in our system we observe dormant origin firing, we
425 speculate that the limiting DNA replication factors are those downstream of origin firing, such as
426 PCNA, RFC and DNA polymerases[55]. Future studies will be aimed at exploring this possibility, with
427 the goal of elucidating the contributions of those factors in DNA replication of aneuploid cells. This
428 line of study might also open novel therapeutic interventions through selective targeting of aneuploid
429 cancer cells by targeting those limiting DNA replication factors.

430 Along this line, another important implication of our finding that DDK and MiDAS play a central
431 role in helping cells coping with aneuploidy is that these mechanisms could well be targetable
432 vulnerabilities of aneuploid cancers. Although it might be challenging to selectively target MiDAS -
433 its key players SLX4-MUS81, RAD52 and POLD3[39,40] are also involved in other processes beyond
434 MiDAS, such as homologous recombination (HR) repair and canonical S-phase DNA replication –
435 things could be different for DDK. In particular, the DDK inhibitor TAK-931 was recently tested in

436 a phase 2 clinical trial for the treatment of advanced solid tumors[56]. Based on our study, we speculate
437 that this drug (and similar ones) could be combined with inhibitors of DNA repair, such as the
438 products of genes playing a role in HR repair, since they were the most differentially regulated in our
439 analysis (Extended Data Table 1). Thus, the combined inhibition of DDK and HR repair factors could
440 potentially be effective to treat aneuploid cancers. This approach would have the great advantage of
441 being highly selective against cancer aneuploid cells, lowering the side-effects of the DNA repair-
442 based cancer therapies and the frequent chemoresistance associated with them[57].
443 In summary, by providing a detailed characterization of the short-term effects of unbalanced
444 karyotypes in the acquisition of aggressive cancer-like features, we demonstrate that aneuploidy
445 provides a point mutation-independent source of genome instability. Although this might offer a
446 source of karyotypic variations capable of enabling proliferative capacity of cancer cells, it also leads
447 to extensive DNA damage. Thus, we speculate that aneuploidy-induced genome instability might be
448 a double-edged sword for cancer cells. On one hand, it is crucial for providing genome plasticity, on
449 the other it might be extremely deleterious because of continuous DNA damage and replication stress.
450 We propose that cancer cells solve this issue by limiting DNA damage - through upregulation of
451 DNA repair genes - to a level compatible with cell proliferation. At the same time, this allows them
452 to keep some degree of genomic instability and thus to continuously sample diverse karyotypic
453 landscapes. Our observations shed new light on the bidirectional association between aneuploidy and
454 genomic instability and propose new approaches for the selective eradication of aneuploid tumors.
455

456 # Methods

457 **Cell culture conditions**

458 The following hTERT RPE-1 cells were all tested free of mycoplasma contamination using Myco
459 Alert (Lonza) according to manufacturer's instructions: hTERT RPE-1 cells, hTERT RPE-1 cells
460 expressing H2b-RFP and PCNA-GFP or H2b-GFP or LCK-GFP (all generated in house), hTERT
461 RPE-1 expressing PCNA-chromobodies and RNF168-miRFP (generated by Dr Simon Gemble and
462 subsequently infected with H2b-GFP), Fluorescent Ubiquitination-based Cell Cycle Indicator
463 (FUCCI) RPE-1 (kind gift of Professor Simona Polo, IFOM, Milan, Italy), hTERT RPE-1 expressing
464 wild-type (wt) or analog-sensitive (as) Cdc7 (kind gift of Professor Prasad V. Jallepalli, MSKCC,
465 New York, USA). All the cells were maintained in a humified environment at 37 degrees with 5%
466 CO_2 and cultured in Dulbecco's modified Eagle's medium (DMEM) or DMEM:F-12 (1:1 ratio)
467 supplemented with 10% fetal bovine serum and 1% penicillin/streptomycin.
468

469 **Cell synchronization and treatments**

470 To harvest cells for FACS analysis, hTERT RPE-1 cells were incubated with thymidine (5mM, Merck
471 Millipore) for 24 hours or with mimosine (0,5mM, Merck Millipore)/aphidicolin (400nM, Merck
472 Millipore)/RO3306 (7,5µM Merck Millipore) for 18 hours, washed 3 times in 1XPBS and harvested
473 after 3,6, 12, 18 or 24 hours.
474 To harvest metaphase cells for mFISH analysis, hTERT RPE-1 cells were synchronized at the G1/S
475 boundary with thymidine, washed 3 times in 1XPBS (washout) and pulsed with the Mps1 inhibitor
476 reversine (500nM, Cayman Chemical) or the vehicle control (dimethyl sulfoxide, DMSO) for 24
477 hours and then harvested for karyotype analysis either immediately after the pulse ('1st mitosis') or
478 24 hours later ('2nd mitosis'). In both cases, colcemid (100ng/ml, Merck Millipore) was added 2 hours
479 before harvesting the cells in order to block cells in prometaphase. To perform ultra-structural
480 analysis of replication intermediates and analyze replication dynamics, cells were treated as above
481 and analyzed immediately after the 24-hour reversine/DMSO pulse.
482 To analyze DNA replication stress markers in S-phase, hTERT RPE-1 cells or hTERT RPE-1 cells
483 expressing wt or as Cdc7 were plated onto fibronectin (5µg/ml, Sigma-Aldrich) coated coverslips at
484 approximately 30% confluence and synchronized with thymidine for 24 hours. After washout, cells
485 were pulsed for 18 hours with reversine or AZ3146 (2µM, Tocris) or vehicle control (DMSO) and
486 released in the presence of mimosine for 18 hours. After washout, cells were incubated for 6 hours in
487 the presence or absence of aphidicolin or the DDK inhibitor XL413 (10µM, Aurogene) or the PP1
488 analog II 1-NM-PP1 (Cayman Chemical) prior to fixation for immunofluorescence. The thymidine
489 analog ethynyl deoxy-uridine (EdU) was added at a final concentration of 10µM during the last 30
490 minutes to label S-phase cells. To check levels of MCM2 phosphorylation in hTERT RPE-1 Cdc7 wt
491 or as cells, after 24h treatment with mimosine, cells were released and allowed to progress in S-phase
492 in the presence or absence of 1-NM-PP1. 6 hours later, they were harvested for Western blot analysis.
493 To assess viability in aneuploid and control cells, hTERT RPE-1 cells were synchronized with
494 thymidine for 24 hours, washed 3 times in 1XPBS and pulsed with reversine/DMSO for 24 hours.
495 Viability was assessed by FACS analysis 120 hours after the reversine/DMSO washout. Cells treated
496 with staurosporin (500nM, Aurogene) for 24 hours were used as a positive control for cell death.
497 To assess S-phase length and quality of the subsequent mitosis by time-lapse microscopy, after
498 plating onto a fibronectin-coated glass 12wellplate, hTERT RPE-1 H2b-RFP and PCNA-GFP cells
499 were blocked in G1/S with thymidine for 24 hours, then washed out, pulsed with reversine/DMSO
500 for 18 hours and filmed for 72 hours.
501 For MiDAS detection, hTERT RPE-1 cells were treated as above and, after reversine/DMSO
502 washout, released in RO3306 for 12 hours to arrest them in late G2 phase. Then, after 3 washes in
503 1XPBS, cells were released in mitosis in the presence of EdU 40µM and colcemid for 2 hours to

504 harvest prometaphase cells for MiDAS detection. Aphidicolin 400nM was added to a subpopulation
505 of cells pulsed with DMSO just after DMSO washout in order to induce DNA replication stress
506 (positive control). To investigate the consequences of MiDAS inhibition in G1 cells, cells were plated
507 and treated as above. After RO3306 washout, cells were released in EdU 40μM in the presence or
508 absence of aphidicolin (2μM, Merck Millipore) for 40 minutes (for prometaphase cells) or 3 hours
509 (for G1 cells) prior to fixation of immunofluorescence. For POLD3 knock-down experiments, hTERT
510 RPE-1 cells were first transfected with POLD3 or scramble siRNAs and then re-plated onto
511 fibronectin-coated coverslips and treated as above. An aliquot of the samples was harvested for
512 Western blot analysis to check the levels of POLD3.
513 In order to harvest daughter pseudo-G1 cells, after thymidine and reversine pulses, hTERT RPE-1
514 LCK-GFP cells were released in the presence or absence of XL413 10μM and arrested in late G2
515 phase with RO3306. After drug washout, cells were incubated in the presence or absence of
516 aphidicolin 2μM for 3 hours together with cytochalasin B (3μg/ml, Merck Millipore) to block
517 cytokinesis prior to fixation for immunofluorescence.
518 To obtain metaphase-like spreads from G1 cells, calyculin A (50ng/ml, Sigma-Aldrich) was added
519 for 45 minutes to G1 cells treated as above to induce premature chromosome condensation, prior to
520 harvest for mFISH analysis.
521 To evaluate β-galactosidase positivity in aneuploid cells, after reversine washout, hTERT RPE-1 cells
522 were allowed to progress for about 60 hours before fixation. The same protocol was used to generate
523 aneuploid cells for sorting, including hTERT FUCCI RPE-1 and hTERT RPE-1 H2b-GFP cells. After
524 sorting, some cells were replated and fixed 16 hours later to perform β-galactosidase staining, while
525 some others were replated for live cell imaging experiments or directly harvested as frozen pellets for
526 RNA extraction. As a positive control for senescence, cells continuously treated with doxorubicin
527 (200nM, Merck Millipore) for 7 days were used.
528
529 **Fluorescence-activated cell sorting (FACS) analysis**
530 hTERT RPE-1 cells were treated as above, harvested, centrifuged and washed once in 1% bovine
531 serum albumin (BSA) in 1XPBS. Cells were fixed in 100% ethanol (added dropwise while vortexing)
532 and stored at +4 degrees overnight. Cells were centrifuged again and stained with staining solution -
533 propidium iodide (20μg/ml, Biotium), RNase A (1mg/ml, Roche) in 1XPBS- for 3 hours at room
534 temperature (RT) prior to FACS analysis.
535 For assessing cell viability, hTERT RPE-1 cells were treated as above, harvested, centrifuged and
536 resuspended in a Zombie Green™ Fixable Viability Kit (BioLegend) 1:100 in 1XPBS for at least 30
537 minutes at RT in the dark. Cells were centrifuged again and resuspended in 1XPBS.

538 In both cases, FACS was carried out on a FACS Celesta BD™ (laser 488, filter 695/40nm for
539 propidium iodide; laser 488, filter 530/30nm for Zombie Green). For each condition, at least 20,000
540 events were recorded, and data analysis was performed using the FlowJo software (v10.7.2). Cells
541 were gated for singlets (as shown in Extended Data Fig.1b) and then, for Zombie Green stained cells,
542 FITC intensity was used to distinguish live from dead cells (as shown in Extended Data Fig.3i), *i.e.*
543 the percentage of live cells was obtained subtracting debris and Zombie-positive cells (*i.e.* dead cells)
544 from the total.
545
546 **Multicolor fluorescence in situ hybridization (mFISH)**
547 After the treatments described above, hTERT RPE-1 cells blocked in prometaphase or G1 cells in
548 which premature condensation was induced were trypsinized and centrifuged to obtain cell pellets.
549 Cell pellets were resuspended in KCl 75mM and incubated for 10 min in a 37 degrees waterbath.
550 After centrifugation, cells were fixed in freshly-prepared Carnoy solution (methanol-acetic acid in a
551 3:1 ratio) while vortexing and then incubated for 30 minutes at RT. After a wash in freshly-prepared
552 Carnoy solution, minimum volume of fixative was left to resuspend the pellet and cells were dropped
553 onto glass slides. mFISH staining was performed following manufacturer's instructions
554 (MetaSystems). The Metafer imaging platform (MetaSystems) and the Isis software (MetaSystems,
555 version 5.5) were used for automated acquisition of the chromosome spread and mFISH image
556 analysis.
557
558 **Ultra-structural analysis of replication intermediates**
559 hTERT RPE-1 cells were treated as above and harvested. Immediately after, cells were psoralen-
560 crosslinked *in vivo* to stabilize replication intermediates as described in[58]. The cell suspension was
561 first incubated with 30 µg/ml 4, 5′, 8-trimethylpsoralen (2mg/ml, Sigma) for 5 min in the dark and
562 then exposed to 365 nm UV light for 8 min in a UV Stratalinker 1800, (Stratagene), with 365 nm UV
563 bulbs (model UVL-56, UVP) at 2–3 cm from the light source. The incubation and irradiation steps
564 were repeated three more times (4 cycles total). Genomic DNA (gDNA) was extracted with phenol-
565 chloroform as described in[58]. 50 µg of gDNA were digested with KpnI and passed through a QIAGEN
566 Genomic-tip 20/G column (QIAGEN) to enrich for replication intermediates, as described by
567 Zellweger and Lopes[59]. EM spreads and imaging was performed as described in[60].
568
569 **Immunofluorescence analysis and EdU detection**
570 At the end of the treatments described above, hTERT RPE-1, hTERT RPE-1 Cdc7 wt or as, or
571 hTERT RPE-1 LCK-GFP cells were washed once in 1XPBS and then fixed in 4% paraformaldehyde

572 (PFA) for 15 minutes at RT. After 3 washes in 1XPBS, cells were blocked in 3% BSA + 0.5% Triton-
573 X in 1XPBS for 30 minutes and incubated with the following primary antibodies diluted in the same
574 buffer for 90 minutes at RT: anti-FANCD2 (NB 100-182, Novus Biologicals) 1:200, anti-RPA
575 (ab2175, Abcam) 1:200, anti-pChk1 (#133D3, Cell Signaling Technology) 1:50, anti-53BP1
576 (ab175933, Abcam) 1:1000, anti-γH2AX (JBW301, Millipore) 1:400. After 3 washes in 1XPBS, cells
577 were incubated with secondary antibodies (ThermoFisher Scientific) diluted 1:400 in 3% BSA + 0.5%
578 Triton-X in 1XPBS for 45 minutes at RT in the dark. Coverslips were then mounted on glass slides
579 using Vectashield Antifade Mounting Medium with DAPI (Vectorlabs).
580 Where indicated, immunofluorescence was combined with EdU detection. Briefly, after the blocking,
581 EdU detection was performed using the Click-iT EdU Cell Proliferation kit for Imaging
582 (ThermoFisher Scientific) following the manufacturer's instructions. After the washes, incubation of
583 the cells in primary antibodies and the subsequent steps of immunofluorescence were performed as
584 above.
585 In all cases, images were acquired using Leica DM6B (Multi Fluo) or Leica SP5 microscope (63x
586 objective was used in both cases).
587
588 **DNA fiber analysis**
589 Cells were labeled sequentially with IdU (green [G]) and CldU (red [R]) and were harvested and
590 processed as described in[14]. Data was collected from 2 independent experiments. A total of 47 and
591 54 Mb of DNA and 33 and 38 Mb of DNA was collected from the control and the aneuploid cells,
592 respectively. Data analysis was performed as described in detail in[24]. Please note that the order of
593 labeling is reversed (CldU→IdU) in the experiments described in[24], therefore, the interpretation of
594 patterns is also reversed as compared to this article. Briefly, origin firing rate is the total number of
595 origins that fired during the first and the second analog in each fiber divided by the total length of
596 the un-replicated DNA in that fiber and the total length of the analog labeling pulses (120 minutes).
597 Origins that fire during the first analog will appear as Red-Green-Red [RGR] and origins that fire
598 during the second analog will appear as Red [R] events. However, origins that fire during the first
599 analog will appear as RGR only if both the forks progress into the second analog. The origins will
600 appear as RG or GR if either of the fork stalls or as G if both the forks stall. Thus, the total number
601 of origins in each fiber was estimated by accounting for the probability of forks stalling.
602 Fork density is the total number of forks in each fiber divided by the total length of the un-replicated
603 DNA of that fiber. Origins and termination events account for 2 forks each and unidirectional fork
604 events account for 1 fork each. However, some of the unidirectional forks could be an origin whose
605 left or rightward fork is stalled. Thus, the total number of forks on each fiber was estimated by

606 accounting for the probability of forks stalling. Please see[24] for calculation of fork stall rate and how
607 the probability of fork stalling was used to estimate the final origin firing rate and fork density for
608 each fiber.
609
610 **Cell proliferation assay**
611 After thymidine synchronization and 18h reversine/DMSO pulse as above, hTERT RPE-1 cells were
612 trypsinized, counted and plated into a 96wellplate in the presence of XL413 10μM or the vehicle
613 control (DMSO). Drugs were re-added fresh every 48-72 hours during the 120 hour -treatment. Then,
614 cell viability was assessed by using the CellTiter-Glo Luminescent cell viability assay (Promega)
615 following manufacturer's instructions.
616
617 **Western blot analysis**
618 hTERT RPE-1 Cdc7 wt or as cells or hTERT RPE-1 cells treated as above were harvested and lysed
619 using RIPA buffer (1x, Cell Signaling Technology) supplemented with protease inhibitor cocktail
620 (Roche) and phosphatase inhibitor cocktail (Merck Millipore) for 15 minutes on ice. After sonication,
621 whole cell lysates were quantified and aliquots of samples were resolved on a Criterion TGX Stain-
622 Free precast gel (Bio-Rad). The membrane was blocked in 1XPBS + 0,1% Tween (1XPBS-T) with
623 non-fat dry milk (5%, Merck Millipore) for 30 minutes at RT and then incubated for 3 hours at RT
624 with a primary antibody resuspended in 1XPBS-T with 5% milk. Following 3x10 minutes washes
625 using 1XPBS-T, the membrane was incubated for 45 minutes at RT with a HRP-conjugated
626 secondary antibody re-suspended in 1XPBS-T, followed by 3x10 minutes washes in PBS-T. Clarity
627 Western ECL Substrate (Bio-Rad) was used for signal detection, and images were captured on a
628 ChemiDoc XRS+ (Bio-rad). Primary antibodies used were: MCM2 (1:1000, A300-191A, Bethyl
629 Laboratories), phosphoS40MCM2 (1:1000, ab133243, Abcam), POLD3 (1:1000, ab182564,
630 Abcam), GAPDH (1:2000, #2118, Cell Signaling Technology) and vinculin (1:5000, V9131, Merck
631 Millipore).
632
633 **Live cell imaging**
634 To monitor S-phase length and M phase duration and quality, hTERT RPE-1 cells were treated as
635 above. After reversine/DMSO washout, fresh medium without phenol red was added to the cells.
636 Cells were imaged every 10 minutes for 72 hours using a 20x/0.75 NA objective with an inverted
637 Nikon Eclipse Ti microscope equipped with an incubator for live cell imaging. The same microscope
638 and acquisition settings were used to film hTERT RPE-1 H2b-GFP aneuploid cycling cells after
639 sorting for 72 hours to assess their genome stability and to film hTERT RPE-1 expressing PCNA-

640 RFP, RNF168-miRFP and H2b-GFP, with the only exception that in the latter case cells were imaged
641 for 110 hours (only miRFP and GFP channels were acquired).
642
643 **MiDAS detection**
644 To detect MiDAS on metaphase spreads, after incubation in EdU and colcemid as above, cells were
645 treated similarly to those for mFISH analysis. After cell dropping onto glass slides and complete
646 evaporation of the Carnoy solution, slides washed in 1XPBS in agitation. EdU detection was
647 performed with the Click-iT EdU Cell Proliferation kit for Imaging (ThermoFisher Scientific)
648 according to manufacturer's instructions with some minor modifications as described in[61]. Slides
649 were then mounted using Vectashield Antifade Mounting Medium with DAPI.
650 To detect MiDAS on prometaphase cells, at the end of the treatments described above, cells were
651 fixed in 4% PFA for 15 minutes at RT, then washed 3 times in 1XPBS. EdU detection was performed
652 as above[61] and coverslips were then mounted on glass slides using the same mounting medium as
653 above.
654 In both cases, images were acquired using Leica DM6B (Multi Fluo) or Leica SP5 microscope (63x
655 objective was used in both cases).
656
657 **RNA interference**
658 hTERT RPE-1 cells were transfected with POLD3 (Ambion) or non-targeting (Dharmacon)
659 smartPool siRNAs at a final concentration of 80nM by using Lipofectamine RNAiMax transfection
660 reagent (Thermo Fisher Scientific) according to the manufacturer's instructions.
661
662 **Telomeric FISH**
663 A Cy3-labeled, C-rich PNA telomere probe (Panagene) was used for telomeric FISH on metaphase
664 spreads according to manufacturer's instructions with minor modifications. At the end of the FISH
665 protocol, EdU detection was performed as indicated above. Slides were mounted as above and images
666 were acquired using Leica DM6B (Multi Fluo) microscope (63X objective).
667
668 **Analysis of distribution of DNA damage in fixed-pseudo-G1 cells**
669 First, the number of FANCD2 and γH2AX foci per daughter cell was counted. Based on the average
670 number of foci per cell, cells with less than 6 or 4 foci (for FANCD2 or γH2AX, respectively) were
671 excluded from the analysis. Then, the total number of foci between the two daughters (*e.g.* 13+10)
672 was calculated and divided by 2 to obtain the number of foci predicted to be inherited by each
673 daughter cell in case of symmetric distribution of DNA damage (*e.g.* 23 divided by 2 is equal to 11,5).

674 Subtraction or addition of this number to the total number of foci in the daughters was used to set a
675 threshold for asymmetric distribution of DNA damage, *e.g.* 23-11,5= 11,5, which is the lowest
676 threshold; 23+11,5= 34,5, which is the highest threshold; if a daughter cell has less than 11,5 or more
677 than 34,5 foci the distribution of DNA damage is considered as non-random (non-random
678 distribution, NDD).
679
680 **Analysis of distribution of DNA damage in live G1 cells**
681 Transmission of DNA damage and its distribution pattern at each cell division were assessed in
682 newly-born G1 hTERT RPE-1 cells expressing PCNA-chromobodies, RNF168-miRFP and H2b-
683 GFP. RNF168 foci were counted 12-24 frames after the end of cell division, *i.e.* when DNA started
684 to decondense, which correspond to 2-4 hours in the G1 phase. First, the frequency of cell divisions
685 with DNA damage transmission was calculated as the percentage of divisions in which daughter cells
686 inherit DNA damage over the total number of cell divisions, independently of its distribution pattern.
687 Second, the frequency of cell divisions in which DNA damage was asymmetrically partitioned was
688 calculated as the percentage of divisions in which daughter cells inherit an unequal number of
689 RNF168 foci (typically 1:0 or 2:1 split) over the total number of cell divisions. Because cells dividing
690 approximately every 24 hours would divide about 5 times during an almost 120 hour-timelapse
691 experiment and aneuploid cells are known to cycle at a slower rate, a cut-off at 4 cell divisions was
692 set in order to distinguish cells with different proliferative capacity: cells undergoing less than 4
693 mitoses would be classified as cells with 'low' proliferative capacity, while cells undergoing at least
694 4 mitoses would be named as cells with 'high' proliferative capacity.
695
696 **β-galactosidase staining**
697 DMSO- and reversine-pulsed cells allowed to progress for either 24, 48 or 72 hours after
698 DMSO/reversine washout, together with sorted cycling and arrested aneuploid cells (when indicated),
699 were plated into a 6 well plate at $1x10^6$ cells/well and allowed to attach overnight. Then, cells were
700 stained using the Senescence β-Galactosidase Staining Kit (Cell Signaling Technology) following
701 manufacturer's instructions and images were acquired using the EVOS imaging system (Thermo
702 Fisher Scientific).
703
704 **Sorting of aneuploid cells**
705 Cells were plated into 150 mm plates (900.000 cells/plate) and treated as above. After
706 reversine/DMSO washout, cells were allowed to divide for about 60 hours. Then, they were incubated
707 with the fluorescent substrate of the β-galactosidase enzyme DDAO-Galactoside (DDAOG) 10mM

708 for 90 minutes. At the end of the incubation, cells were harvested for FACS sorting and acquired
709 using a FACSAria Fusion flow cytometer (BD). Cells were first gated for singlets and alive cells
710 (based on DAPI staining); then, FSC-A and Alexa-647 intensity were used to distinguish cycling
711 from arrested cells, *i.e.* cycling cells were gated using the same Alexa-647 Mean Fluorescence
712 Intensity of the control sample without DDAOG, while arrested cells were gated imposing 0,1% or
713 0,5% on Alexa-647 signal to the control sample without DDAOG. FlowJo was used to perform data
714 analysis and generate the plots in Fig. 5 and Extended Data Fig. 7.
715
716 **Cell cycle profile analysis through the FUCCI system**
717 hTERT FUCCI RPE-1 cells were used to generate euploid, aneuploid, cycling aneuploid and arrested
718 aneuploid cells as described above. After the sorting, cells were plated in a 12wellplate, allowed to
719 attach overnight and then filmed using an inverted Nikon Eclipse Ti microscope with a 20x/0.75 NA
720 objective equipped with an incubator for live cell imaging. Brightfield, green (GFP) and red
721 (mCherry) channels were used to acquire the movie. Images were taken every 30 minutes for 24
722 hours. Cell cycle stage was determined based on nuclear color: red nuclei were scored as G1 phase,
723 while yellow and green nuclei were scored as S/G2 phase; lastly, M phase was characterized by
724 uncolored nuclei of two dividing cells[49].
725
726 **Sample processing for RNAseq**
727 Aneuploid cycling and arrested cells post sorting were centrifuged and cell pellets were obtained.
728 RNA was extracted from them using a RNeasy kit (QIAGEN) and its quality was assessed with a
729 Bioanalyzer 2100 (Agilent). Then, for each sample, total RNA was depleted of ribosomal RNA and
730 the RNAseq libraries were prepared with the Illumina TruSeq Stranded Total RNA kit following the
731 manufacturer's protocol. Briefly, after the fragmentation of RNA using divalent cations at elevated
732 temperature, cDNA was synthesized, end-repaired and 3'-end-adenylated. Following adapter
733 ligation, libraries were amplified by PCR. Amplified libraries were checked on a Bioanalyzer 2100
734 (Agilent) and quantified with picogreen reagent. Libraries with distinct TruSeq adapter UDIndexes
735 were sequenced for 50 bases in the paired-end mode with 35 million reads in coverage on a Novaseq
736 6000 sequencer.
737
738 **Data analysis of RNAseq**
739 RNA reads were aligned to the GRCh38 primary assembly with Ensembl 104[62] gene annotations
740 using. STAR 2.7.9a[63]. Gene counts were quantified with subread 2.0.2[64]. Differentially expressed
741 genes were determined using DESeq2 1.30.0[65] with a Wald test, regressing out for the batch factor.

742 Subsequently, genes were filtered based on significance (p-value ≤0.05 and pADJ ≤0.25; for the
743 aneuploid *vs.* control analysis results were filtered only based on p-value). Pre-ranked gene set
744 enrichment analysis (PreRanked GSEA) was performed to identify enriched pathways[66]. Single cell
745 gene set enrichment analysis (ssGSEA) was performed using GenePatterns[66,67], to compare the
746 expression of specific DNA damage-related signatures across samples. Z-scores were calculated for
747 each gene signature across and plotted as a heatmap. Plots were generated using the Python's
748 'seaborn' library (Van Rossum and Drake, 2009).
749
750 **Kinetics of DNA repair upon exposure to IR**
751 After cell sorting (as described above), aneuploid cycling and arrested cells, together with non-sorted
752 aneuploid cells and euploid controls, were plated on coverslips and incubated overnight. The day
753 after, cells were γ-irradiated (1.25Gy) with the Faxitron CP-160 (Faxitron x-ray Corporation) and
754 fixed for immunofluorescence as indicated above at different timepoints. In order to exclude S-phase
755 cells, cells were pulsed with EdU 10μM for 30 minutes before fixation. Non-irradiated cells were
756 fixed together with the first timepoint. *i.e.* 0h post irradiation. For each sample, the number of γH2AX
757 foci/53BP1 bodies per cell was counted, their average per cell was calculated and normalized to that
758 at 0h post irradiation.
759
760 **Association of DDR gene expression with doubling time**
761 CCLE (Cancer cell line encyclopedia) gene expression data were obtained from DepMap
762 (https://depmap.org/portal/) 22Q1 release[52] and cell line doubling times were obtained from[51]. Cell
763 lines were divided to quartiles according to their doubling time, while ssGSEA scores were generated
764 using the GenePattern platform (https://www.genepattern.org/)[66,67] and compared between the top
765 and bottom quartiles. Statistical analysis (two-tailed Student' t-test) and plotting were performed
766 using GraphPad PRISM v9.3.1.
767
768 **Sample processing for single-cell whole genome sequencing (scWGS)**
769 Cell pellets were resuspended in cell lysis buffer (100mM Tris-HCl pH 7.4, 154mM NaCl, 1mM
770 $CaCl_2$, 500μM $MgCl_2$, 0,2% BSA, 0,1% NP-40, 10μg/ml Hoechst 33358, 2μg/ml propidium iodide
771 in ultra-pure water) and incubated on ice in the dark for 15 minutes to ensure complete lysis. Resulting
772 single nuclei of G1 phase (as determined by Hoechst and PI staining) were sorted into single wells of
773 96 wellplates on a MoFlo Astrios cell sorter (Beckman Coulter) and sorted at -80 degrees until further
774 processing. Automated library preparation was performed (Bravo Automated Liquid Handling

775 Platform, Agilent Technologies) as previously described[68]. Resulting single-cell libraries were pooled
776 for subsequent sequencing.
777
778 **Data analysis for scWGS**
779 Sequencing was performed using a NextSeq 500 machine (Illumina; up to 77 or 68 cycles – single
780 end; excluding sample-specific barcodes). Reads were afterwards aligned to the human reference
781 genome (GRCh38/hg38) using Bowtie2 (version 2.2.4 or 2.3.4.1;[69]). Duplicate reads were marked
782 with BamUtil (version 1.0.3;[70]) or Samtools markdup (version 1.9;[71]. The aligned read data (bam
783 files) were analyzed with a copy number calling algorithm called AneuFinder
784 (https://github.com/ataudt/aneufinder;[72]). Following GC correction and blacklisting of artefact-prone
785 regions (extreme low or high coverage in control samples), libraries were analyzed using the dnacopy
786 and edivisive copy number calling algorithms with variable width bins (average bin size = 1 Mb; step
787 size = 500 kb). Results were afterwards curated by requiring a minimum concordance of 95% between
788 the results of the two algorithms. Libraries with on average less than 10 reads per bin (~ 55,000 reads
789 for a diploid genome) were discarded. A chromosome was classified as aneuploid when at least 95
790 % of the bins showed a deviation from euploid (deviation from 2-somy). Chromosomes 10 and 12
791 were excluded for the calculation of whole-genome scores.
792
793 **Image analysis**
794 After acquisition, microscopy images were analyzed with Fiji or Arivis software and processed with
795 Fiji or Huygens software. Details of image processing, where applicable, are annotated in figure
796 legends.
797
798 **Quantification and statistical analysis**
799 All statistical analyses were performed using GraphPad Prism software (9.2.0 version). Statistical
800 significance in each case was calculated using two-tailed Student's t-test, Chi-squared test or Fisher's
801 exact test. Where not indicated on the graphs, differences were not statistically significant. The details
802 of error bars, number of biological replicates and *n* for each experiment are annotated in figure
803 legends.
804
805 ## Data availability
806 RNAseq and scWGS data generated during this study have been deposited at the EMBL-EBI
807 repositories ENA and ArrayExpress with the following accession numbers E-MTAB-12537 and

808 PRJEB58407, respectively. The remaining data are available within the Article, Extended Data or
809 Source Data file. Source data are provided with this paper.
810

811 **References**

812 1. Santaguida S, Amon A. Short- and long-term effects of chromosome mis-segregation and
813 aneuploidy. *Nat Rev Mol Cell Biol*. 2015;16(8):473-485. doi:10.1038/nrm4025
814 2. Ben-David U, Amon A. Context is everything: aneuploidy in cancer. *Nat Rev Genet*.
815 2020;21(1):44-62. doi:10.1038/s41576-019-0171-x
816 3. Ippolito MR, Martis V, Martin S, et al. Gene copy-number changes and chromosomal
817 instability induced by aneuploidy confer resistance to chemotherapy. *Dev Cell*.
818 2021;56(17):2440-2454.e6. doi:10.1016/j.devcel.2021.07.006
819 4. Lukow DA, Sausville EL, Suri P, et al. Chromosomal instability accelerates the evolution of
820 resistance to anti-cancer therapies. *Dev Cell*. 2021;56(17):2427-2439.e4.
821 doi:10.1016/j.devcel.2021.07.009
822 5. Shoshani O, Bakker B, De Haan L, et al. Transient genomic instability drives tumorigenesis
823 through accelerated clonal evolution. *Genes Dev*. 2021;35(15-16):1093-1109.
824 doi:10.1101/gad.348319.121
825 6. Trakala M, Aggarwal M, Sniffen C, et al. Clonal selection of stable aneuploidies in
826 progenitor cells drives high-prevalence tumorigenesis. *Genes Dev*. 2021;35(15-16):1079-
827 1092. doi:10.1101/gad.348341.121
828 7. Ohashi A, Ohori M, Iwai K, et al. Aneuploidy generates proteotoxic stress and DNA damage
829 concurrently with p53-mediated post-mitotic apoptosis in SAC-impaired cells. *Nat Commun*.
830 2015;6. doi:10.1038/ncomms8668
831 8. Santaguida S, Vasile E, White E, Amon A. Aneuploidy-induced cellular stresses limit
832 autophagic degradation. *Genes Dev*. 2015;29(19):2010-2021. doi:10.1101/gad.269118.115
833 9. Stingele S, Stoehr G, Peplowska K, Cox J, Mann M, Storchova Z. Global analysis of
834 genome, transcriptome and proteome reveals the response to aneuploidy in human cells. *Mol*
835 *Syst Biol*. 2012;8(608). doi:10.1038/msb.2012.40
836 10. Williams BR, Prabhu VR, Hunter KE, et al. and Spontaneous Immortalization. *October*.
837 2008;322(October):703-710.
838 11. Torres EM, Sokolsky T, Tucker CM, et al. Effects of aneuploidy on cellular physiology and
839 cell division in haploid yeast. *Science (80-)*. 2007;317(5840):916-924.
840 doi:10.1126/science.1142210
841 12. Sheltzer JM, Blank HM, Pfau SJ, et al. Aneuploidy drives genomic instability in yeast.

842 *Science (80-)*. 2011;333(6045):1026-1030. doi:10.1126/science.1206412
843 13. Passerini V, Ozeri-Galai E, De Pagter MS, et al. The presence of extra chromosomes leads to
844 genomic instability. *Nat Commun*. 2016;7. doi:10.1038/ncomms10754
845 14. Santaguida S, Richardson A, Iyer DR, et al. Chromosome Mis-segregation Generates Cell-
846 Cycle-Arrested Cells with Complex Karyotypes that Are Eliminated by the Immune System.
847 *Dev Cell*. 2017;41(6):638-651.e5. doi:10.1016/j.devcel.2017.05.022
848 15. Davoli T, Xu AW, Mengwasser KE, et al. XCumulative haploinsufficiency and
849 triplosensitivity drive aneuploidy patterns and shape the cancer genome. *Cell*.
850 2013;155(4):948. doi:10.1016/j.cell.2013.10.011
851 16. Garribba L, Santaguida S. The Dynamic Instability of the Aneuploid Genome. *Front Cell*
852 *Dev Biol*. 2022;10. doi:10.3389/fcell.2022.838928
853 17. Blank HM, Sheltzer JM, Meehl CM, Amon A. Mitotic entry in the presence of DNA damage
854 is a widespread property of aneuploidy in yeast. *Mol Biol Cell*. 2015;26(8):1440-1451.
855 doi:10.1091/mbc.E14-10-1442
856 18. Burrell RA, McClelland SE, Endesfelder D, et al. Replication stress links structural and
857 numerical cancer chromosomal instability. *Nature*. 2013;494(7438):492-496.
858 doi:10.1038/nature11935
859 19. Wang RW, Viganò S, Ben-David U, Amon A, Santaguida S. Aneuploid senescent cells
860 activate NF-κB to promote their immune clearance by NK cells. *EMBO Rep*. 2021;22(8):1-
861 16. doi:10.15252/embr.202052032
862 20. Cohen-Sharir Y, McFarland JM, Abdusamad M, et al. Aneuploidy renders cancer cells
863 vulnerable to mitotic checkpoint inhibition. *Nature*. 2021;590(7846):486-491.
864 doi:10.1038/s41586-020-03114-6
865 21. Replogle JM, Zhou W, Amaro AE, et al. Aneuploidy increases resistance to
866 chemotherapeutics by antagonizing cell division. *Proc Natl Acad Sci U S A*.
867 2020;117(48):30566-30576. doi:10.1073/pnas.2009506117
868 22. Santaguida S, Tighe A, D'Alise AM, Taylor SS, Musacchio A. Dissecting the role of MPS1
869 in chromosome biorientation and the spindle checkpoint through the small molecule inhibitor
870 reversine. *J Cell Biol*. 2010;190(1):73-87. doi:10.1083/jcb.201001036
871 23. Neelsen KJ, Lopes M. Replication fork reversal in eukaryotes: From dead end to dynamic
872 response. *Nat Rev Mol Cell Biol*. 2015;16(4):207-220. doi:10.1038/nrm3935
873 24. Iyer DR, Rhind N. *Replication Fork Slowing and Stalling Are Distinct, Checkpoint-*
874 *Independent Consequences of Replicating Damaged DNA*. Vol 13.; 2017.
875 doi:10.1371/journal.pgen.1006958

876 25. Lamm N, Ben-David U, Golan-Lev T, Storchová Z, Benvenisty N, Kerem B. Genomic
877 Instability in Human Pluripotent Stem Cells Arises from Replicative Stress and Chromosome
878 Condensation Defects. *Cell Stem Cell*. 2016;18(2):253-261. doi:10.1016/j.stem.2015.11.003
879 26. Ge XQ, Jackson DA, Blow JJ. Dormant origins licensed by excess Mcm2-7 are required for
880 human cells to survive replicative stress. *Genes Dev*. 2007;21(24):3331-3341.
881 doi:10.1101/gad.457807
882 27. Jares P, Blow JJ. Xenopus Cdc7 function is dependent on licensing but not on XORC,
883 XCdc6, or CDK activity and is required for XCdc45 loading. *Genes Dev*. 2000;14(12):1528-
884 1540. doi:10.1101/gad.14.12.1528
885 28. Tanaka S, Umemori T, Hirai K, Muramatsu S, Kamimura Y, Araki H. CDK-dependent
886 phosphorylation of Sld2 and Sld3 initiates DNA replication in budding yeast. *Nature*.
887 2007;445(7125):328-332. doi:10.1038/nature05465
888 29. Labib K. Howdo Cdc7 and cyclin-dependent kinases trigger the initiation of chromosome
889 replication in eukaryotic cells? *Genes Dev*. 2010;24(12):1208-1219.
890 doi:10.1101/gad.1933010
891 30. Heller RC, Kang S, Lam WM, Chen S, Chan CS, Bell SP. Eukaryotic origin-dependent DNA
892 replication in vitro reveals sequential action of DDK and S-CDK kinases. *Cell*.
893 2011;146(1):80-91. doi:10.1016/j.cell.2011.06.012
894 31. Jones MJK, Gelot C, Munk S, et al. Human DDK rescues stalled forks and counteracts
895 checkpoint inhibition at unfired origins to complete DNA replication. *Mol Cell*.
896 2021;81(3):426-441.e8. doi:https://doi.org/10.1016/j.molcel.2021.01.004
897 32. Koltun ES, Tsuhako AL, Brown DS, et al. Discovery of XL413, a potent and selective CDC7
898 inhibitor. *Bioorganic Med Chem Lett*. 2012;22(11):3727-3731.
899 doi:10.1016/j.bmcl.2012.04.024
900 33. Hewitt L, Tighe A, Santaguida S, et al. Sustained Mps1 activity is required in mitosis to
901 recruit O-Mad2 to the Mad1-C-Mad2 core complex. *J Cell Biol*. 2010;190(1):25-34.
902 doi:10.1083/jcb.201002133
903 34. Zeman MK, Cimprich KA. Causes and consequences of replication stress. *Nat Cell Biol*.
904 2014;16(1):2-9. doi:10.1038/ncb2897
905 35. Chan KL, Palmai-Pallag T, Ying S, Hickson ID. Replication stress induces sister-chromatid
906 bridging at fragile site loci in mitosis. *Nat Cell Biol*. 2009;11(6):753-760.
907 doi:10.1038/ncb1882
908 36. Mankouri HW, Huttner D, Hickson ID. How unfinished business from S-phase affects
909 mitosis and beyond. *EMBO J*. 2013;32(20):2661-2671. doi:10.1038/emboj.2013.211

910 37. Wilhelm T, Olziersky AM, Harry D, et al. Mild replication stress causes chromosome mis-
911 segregation via premature centriole disengagement. *Nat Commun*. 2019;10(1):1-14.
912 doi:10.1038/s41467-019-11584-0
913 38. Ellison V, Stillman B. Biochemical characterization of DNA damage checkpoint complexes:
914 Clamp loader and clamp complexes with specificity for 5′ recessed DNA. *PLoS Biol*.
915 2003;1(2). doi:10.1371/journal.pbio.0000033
916 39. Minocherhomji S, Ying S, Bjerregaard VA, et al. Replication stress activates DNA repair
917 synthesis in mitosis. *Nature*. 2015;528(7581):286-290. doi:10.1038/nature16139
918 40. Bhowmick R, Minocherhomji S, Hickson ID. RAD52 Facilitates Mitotic DNA Synthesis
919 Following Replication Stress. *Mol Cell*. 2016;64(6):1117-1126.
920 doi:10.1016/j.molcel.2016.10.037
921 41. Garribba L, Bjerregaard VA, Gonçalves Dinis MM, et al. Folate stress induces SLX1- And
922 RAD51-dependent mitotic DNA synthesis at the fragile X locus in human cells. *Proc Natl*
923 *Acad Sci U S A*. 2020;117(28):16527-16536. doi:10.1073/pnas.1921219117
924 42. Bonner WM, Redon CE, Dickey JS, et al. γH2AX and cancer. *Nat Rev Cancer*.
925 2008;8(12):957-967. doi:10.1038/nrc2523
926 43. Fenech M, Morley AA. Measurement of micronuclei in lymphocytes. *Mutat Res*. 147(1-
927 2):29-36. doi:10.1016/0165-1161(85)90015-9
928 44. Miura T, Blakely WF. Optimization of calyculin A-induced premature chromosome
929 condensation assay for chromosome aberration studies. *Cytom Part A*. 2011;79 A(12):1016-
930 1022. doi:10.1002/cyto.a.21154
931 45. Xing M, Zhang F, Liao H, et al. Replication Stress Induces ATR/CHK1-Dependent
932 Nonrandom Segregation of Damaged Chromosomes. *Mol Cell*. 2020;78(4):714-724.e5.
933 doi:10.1016/j.molcel.2020.04.005
934 46. Rocheteau P, Gayraud-Morel B, Siegl-Cachedenier I, Blasco MA, Tajbakhsh S. A
935 subpopulation of adult skeletal muscle stem cells retains all template DNA strands after cell
936 division. *Cell*. 2012;148(1-2):112-125. doi:10.1016/j.cell.2011.11.049
937 47. Dimri GP, Lee X, Basile G, et al. A biomarker that identifies senescent human cells in
938 culture and in aging skin in vivo. *Proc Natl Acad Sci U S A*. 1995;92(20):9363-9367.
939 doi:10.1073/pnas.92.20.9363
940 48. Macedo JC, Vaz S, Bakker B, et al. FoxM1 repression during human aging leads to mitotic
941 decline and aneuploidy-driven full senescence. *Nat Commun*. 2018;9(1):1-17.
942 doi:10.1038/s41467-018-05258-6
943 49. Sakaue-Sawano A, Kurokawa H, Morimura T, et al. Visualizing Spatiotemporal Dynamics of

944 Multicellular Cell-Cycle Progression. *Cell*. 2008;132(3):487-498.
945 doi:10.1016/j.cell.2007.12.033
946 50. Zerbib J, Ippolito MR, Reuveni E, et al. Aneuploid cells depend on the RAF/MEK/ERK
947 pathway and on RNA degradation for overcoming DNA damage and transcriptional burden.
948 *In_Submission*.
949 51. Tsherniak A, Vazquez F, Montgomery PG, et al. Defining a Cancer Dependency Map. *Cell*.
950 2017;170(3):564-576.e16. doi:10.1016/j.cell.2017.06.010
951 52. Ghandi M, Huang FW, Jané-Valbuena J, et al. Next-generation characterization of the
952 Cancer Cell Line Encyclopedia. *Nature*. 2019;569(7757):503-508. doi:10.1038/s41586-019-
953 1186-3
954 53. Hanahan D. Hallmarks of Cancer: New Dimensions. *Cancer Discov*. 2022;12(1):31-46.
955 doi:10.1158/2159-8290.CD-21-1059
956 54. Gemble S, Wardenaar R, Keuper K, et al. Genetic instability from a single S-phase after
957 whole-genome duplication. *Nature*. 2022;604(7904):146-151. doi:10.1038/s41586-022-
958 04578-4
959 55. Fragkos M, Ganier O, Coulombe P, Méchali M. DNA replication origin activation in space
960 and time. *Nat Rev Mol Cell Biol*. 2015;16(6):360-374. doi:10.1038/nrm4002
961 56. Iwai K, Nambu T, Dairiki R, et al. Molecular mechanism and potential target indication of
962 TAK-931, a novel CDC7-selective inhibitor. *Sci Adv*. 2019;5(5). doi:10.1126/sciadv.aav3660
963 57. Pilié PG, Tang C, Mills GB, Yap TA. State-of-the-art strategies for targeting the DNA
964 damage response in cancer. *Nat Rev Clin Oncol*. 2019;16(2):81-104. doi:10.1038/s41571-
965 018-0114-z
966 58. Mazzucco G, Huda A, Galli M, Zanella E, Doksani Y. Purification of mammalian telomeric
967 DNA for single-molecule analysis. *Nat Protoc*. Published online 2022:1-27.
968 doi:10.1038/s41596-022-00684-9
969 59. Kolstø AB. *Genome Instability*. Vol 106.; 1998. doi:10.1111/j.1600-0463.1998.tb05651.x
970 60. Mazzucco G, Huda A, Galli M, et al. Telomere damage induces internal loops that generate
971 telomeric circles. *Nat Commun*. 2020;11(1). doi:10.1038/s41467-020-19139-4
972 61. Garribba L, Wu W, Özer Ö, Bhowmick R, Hickson ID, Liu Y. Inducing and Detecting
973 Mitotic DNA Synthesis at Difficult-to-Replicate Loci. *Methods Enzymol*. 2018;601:45-58.
974 doi:10.1016/bs.mie.2017.11.025
975 62. Yates AD, Achuthan P, Akanni W, et al. Ensembl 2020. *Nucleic Acids Res*.
976 2020;48(D1):D682-D688. doi:10.1093/nar/gkz966
977 63. Dobin A, Davis CA, Schlesinger F, et al. STAR: Ultrafast universal RNA-seq aligner.

978 *Bioinformatics*. 2013;29(1):15-21. doi:10.1093/bioinformatics/bts635
979 64. Liao Y, Smyth GK, Shi W. FeatureCounts: An efficient general purpose program for
980 assigning sequence reads to genomic features. *Bioinformatics*. 2014;30(7):923-930.
981 doi:10.1093/bioinformatics/btt656
982 65. Love MI, Huber W, Anders S. Moderated estimation of fold change and dispersion for RNA-
983 seq data with DESeq2. *Genome Biol*. 2014;15(12):1-21. doi:10.1186/s13059-014-0550-8
984 66. Subramanian A, Tamayo P, Mootha VK, et al. Gene set enrichment analysis: A knowledge-
985 based approach for interpreting genome-wide expression profiles. *Proc Natl Acad Sci U S A*.
986 2005;102(43):15545-15550. doi:10.1073/pnas.0506580102
987 67. Reich M, Liefeld T, Gould J, Lerner J, Tamayo P, Mesirov JP. GenePattern 2.0. *Nat Genet*.
988 2006;38(5):500-501. doi:10.1038/ng0506-500
989 68. van den Bos H, Bakker B, Taudt A, et al. Quantification of Aneuploidy in Mammalian
990 Systems. *Methods Mol Biol*. 2019;1896:159-190. doi:10.1007/978-1-4939-8931-7_15
991 69. Langmead B, Salzberg SL. Fast gapped-read alignment with Bowtie 2. *Nat Methods*.
992 2012;9:357-359. doi:10.1038/nmeth.1923
993 70. Jun G, Wing MK, Abecasis GR, Kang HM. An efficient and scalable analysis framework for
994 variant extraction and refinement from population-scale DNA sequence data. *Genome Res*.
995 2015;25(6):918-925. doi:10.1101/gr.176552.114
996 71. Danecek P, Bonfield JK, Liddle J, et al. Twelve years of SAMtools and BCFtools.
997 *Gigascience*. 2021;10(2):1-4. doi:10.1093/gigascience/giab008
998 72. Bakker B, Taudt A, Belderbos ME, et al. Single-cell sequencing reveals karyotype
999 heterogeneity in murine and human malignancies. *Genome Biol*. 2016;17(1):1-15.
1000 doi:10.1186/s13059-016-0971-7
1001 73. Zhang CZ, Spektor A, Cornils H, et al. Chromothripsis from DNA damage in micronuclei.
1002 *Nature*. 2015;522(7555):179-184. doi:10.1038/nature14493
1003

1004 ## Acknowledgments

1005 We are very grateful to all the members of the Santaguida lab for fruitful discussions throughout the
1006 project. We thank Elsa Logarinho and members of M. Mapelli lab for constructive discussions, and
1007 Elia Zanella for help with telomeric FISH. We acknowledge help from Flow Cytometry, Genomic
1008 and Imaging units at IEO for their technical assistance. Work in the Santaguida lab is supported by
1009 grants from the Italian Association for Cancer Research (MFAG 2018 - ID. 21665 project), Ricerca
1010 Finalizzata (GR-2018-12367077), Fondazione Cariplo, the Rita-Levi Montalcini program from
1011 MIUR and the Italian Ministry of Health with Ricerca Corrente and 5x1000 funds. L.G. is supported

by a fellowship from Fondazione IEO-Monzino. M.R.I. is supported by an AIRC Fellowship (ID 26738-2021). Work in the Ben-David lab is supported by grants from the European Research Council (ERC grant #945674), Israel Cancer Research Foundation Gesher Award, Israel Science Foundation (ISF grant #1805/21), the DoD CDMRP Career Development Award (grant #CA191148), the Azrieli Faculty Fellowship and the EMBO Young Investigator Program. D.F. receives salary support from the CNRS and I. Curie, M.D. from I. Curie. Work in Fachinetti lab was supported by an Emergence Grant 2018 from the City of Paris.

Author Contributions

LG and GDF performed the vast majority of the experiments, analyzed the data and prepared the figures. VM performed the experiments presented in Fig. 5a-f and contributed to the experiments presented in Extended Data Fig. 1a,b, 2a-f, 3b,i, 4c,d, 7b,e. MG and YD generated the EM data. MD and DF performed the mFISH analyses. YE and UBD analyzed the RNAseq data and CCLE data. RW, AET, DCJS, MS and FF performed the scWGS and RNAseq. MRI performed the viability assay in Fig. 2i. DRI and NR performed the DNA fiber analysis. ST generated the data presented in Extended Data Fig. 7a. CS assisted with live cell imaging experiments. SG and RB provided the hTERT RPE-1 expressing PCNA-chromobodies and RNF168-miRFP. SS conceptualized the study, coordinated the research and wrote the manuscript together with LG and GDF and with input from all the authors.

Competing Interests

The authors declare no competing interests.

Figure legends

Fig. 1: Aneuploid cells accumulate increasing genome instability and display higher levels of DNA replication stress markers in S-phase. a, Experimental setup for the analysis of genome instability of cells obtained from the 1st and the 2nd mitosis. Karyotype aberrations were assessed by mFISH analysis. **b,c,** Representative mFISH images (b) of karyotypes obtained from the 1st (n=68) and the 2nd mitosis (n=98) in aneuploid cells and relative quantification (c). T(10,X) and +12 were excluded from the analysis as they are clonal in hTERT RPE-1 cells. **d,** Quantification of aneuploid

1043 cells with either numerical (W-CIN) or structural (S-CIN) aneuploidy in aneuploid cells obtained
1044 from the 1st (n=68) and the 2nd mitosis (n=98). **e**, Schematic representation of the experimental
1045 approaches used for the study of the 1st S-phase after induction of chromosome missegregation. A
1046 short EdU pulse was performed before cell harvest in order to label S-phase cells to be analyzed by
1047 immunofluorescence. **f,g,** Representative images of normal and reversed replication forks (f)
1048 analyzed by electron microscopy and quantification (g) of the reversed ones in control (n=108) and
1049 aneuploid (n=95) cells. **h,i,** Representative images (h) and quantification (i) of FANCD2 foci per S-
1050 phase cell in control (n=181) and aneuploid (n=148) cells. **j,k,** Representative images (j) and
1051 quantification (k) of RPA foci per S-phase cell in control (n=133) and aneuploid (n=136) cells. **l,m,**
1052 Representative images (l) and quantification (m) of pChk1 foci per S-phase cell in control (n=129)
1053 and aneuploid (n=134) cells. Cells treated with aphidicolin (RS, replication stress) were used as a
1054 positive control (n=144 for panel i, n=137 for panel k and n=131 for panel m). **n,** Representative
1055 images of DNA fiber analysis in control and aneuploid cells. **o,p,** Quantification of fork density per
1056 Mb (o) and origin firing rate (p) per Mb in control (n= 411) and aneuploid (n=425) cells. Ctrl, control
1057 (DMSO pulsed). Aneu, aneuploid cells (Mps1 inhibitor pulsed). RS, replication stress (aphidicolin
1058 treated cells). W-CIN, numerical chromosomal instability. S-CIN, structural chromosomal instability.
1059 Scale bars, 5µm. LUT was inverted for FANCD2, RPA and pChk1 images. Blue borders in images
1060 are based on DAPI staining and define nuclei. Data are means of three biological replicates, except
1061 for the EM (one replicate) and the DNA fiber analysis (two replicates). Chi-squared test was
1062 performed for data in panel c. Two-tailed unpaired Student's t-test was performed for data in panels
1063 i, k, m, o, p. In graphs, average values for each biological replicate are shown by colored dots (each
1064 color corresponds to a different biological replicate). ** denotes p<0,01; **** denotes p <0,001.
1065 Source Data are provided as a Source Data file.
1066
1067 **Fig. 2: DDK protects aneuploid cells from DNA damage accumulation and consequent cell**
1068 **death. a,** Experimental workflow for the analysis of DNA replication stress markers in S-phase cells
1069 upon treatment with the DDK inhibitor XL-413. A short EdU pulse was performed before cell harvest
1070 in order to label S-phase cells. **b,c,** Representative images (b) and quantification (c) of FANCD2 foci
1071 per S-phase cell in control or aneuploid cells ± DDK inhibitor (n=123 for Ctrl, n=125 for Ctrl+DDKi,
1072 n=126 for Aneu, n=137 for Aneu+DDKi). **d,e,** Representative images (d) and quantification (e) of
1073 RPA foci per S-phase cell in control or aneuploid cells ± DDK inhibitor (n=136 for Ctrl, n=134 for
1074 Ctrl+DDKi, n=119 for Aneu, n=118 for Aneu+DDKi). **f,g,** Representative images (f) and
1075 quantification (g) of pChk1 foci per S-phase cell in control or aneuploid cells ± DDK inhibitor (n=127
1076 for Ctrl, n=132 for Ctrl+DDKi; n=131 for Aneu; n=128 for Aneu+DDKi). **h,** Experimental workflow

1077 for the assessment of cell viability upon exposure to the DDK inhibitor. **i,** Quantification of live cells
1078 upon DDK inhibitor treatment in control and aneuploid cells (for each sample, values were
1079 normalized to the untreated control). Ctrl, control (DMSO pulsed). Aneu, aneuploid cells (Mps1
1080 inhibitor pulsed). DDKi, DDK inhibitor. Scale bars, 5µm. LUT was inverted for FANCD2, RPA and
1081 pChk1 images. Blue borders in images are based on DAPI staining and define nuclei. Data are means
1082 of at least three biological replicates. Error bars in panel i represent SEMs. Two-tailed unpaired
1083 Student's t-test was performed for data in panels c, e, g and i. In graphs, average values for each
1084 biological replicate are shown by colored dots (each color corresponds to a different biological
1085 replicate). * denotes p<0,05; *** denotes p< 0,005; **** denotes p<0,001. Source Data are provided
1086 as a Source Data file.
1087
1088 **Fig. 3: MiDAS protects aneuploid cells from a further increase in their genome instability. a,**
1089 Experimental workflow for the analysis of the 1st S-phase duration, 2nd M phase duration and quality
1090 by live-cell imaging in hTERT RPE-1 cells expressing H2b-RFP and PCNA-GFP. **b,** Representative
1091 images from the movies of mitosis duration and quality in control and aneuploid cells. For illustration
1092 purposes, images were deconvoluted by using the Huygens software using the deconvolution express
1093 function. **c,d,** Correlation between (c) S-phase duration and quality of the subsequent mitosis and (d)
1094 mitotic timing and mitotic quality in control (for panel c: n=98 for Ctrl Normal M, n=27 for Ctrl
1095 Abnormal M; for panel d: n=98 for Ctrl Normal M, n=34 for Ctrl Abnormal M) and aneuploid (for
1096 panel c: n=43 for Aneu Normal M, n=63 for Aneu Abnormal M; for panel d: n=43 for Aneu Normal
1097 M, n=62 for Aneu Abnormal M) cells. **e,f**, Representative images (e) and quantification (f) of EdU
1098 incorporation on metaphase spreads in control (n=129) and aneuploid (n=167) cells. Cells treated
1099 with aphidicolin (RS, replication stress) were used as a positive control (n=106). **g,** Experimental
1100 workflow for the assessment of genome instability in the following G1 phase upon MiDAS inhibition.
1101 **h,i,** Representative images (h) and quantification (i) of EdU incorporation in prometaphase cells upon
1102 MiDAS inhibition (n=130 for Ctrl, n=113 for Ctrl+MiDASi, n=156 for Aneu, n=116 for
1103 Aneu+MiDASi). Cells treated with aphidicolin (RS, replication stress) were used as a positive control
1104 (n=111 for RS, n=91 for RS+MiDASi). **j,k,l,** Representative images (j) and quantification of 53BP1
1105 body (k) and micronucleus (l) accumulation in G1 cells following inhibition of MiDAS (for panel k:
1106 n=544 for Ctrl, n=518 for Ctrl + MiDASi, n=543 for Aneu, n=613 for Aneu + MiDASi, n=446 for
1107 RS, n=431 for RS + MiDASi. For panel l: n=556 for Ctrl, n=643 for Ctrl + MiDASi, n=543 for Aneu,
1108 n=641 for Aneu + MiDASi, n=397 for RS, n=416 for RS + MiDASi). Ctrl, control (DMSO pulsed).
1109 Aneu, aneuploid cells (Mps1 inhibitor pulsed). RS, replication stress (aphidicolin treated cells).
1110 MiDASi, MiDAS inhibitor. Normal M, normal mitosis. Abnormal M, abnormal mitosis. Scale bars,

1111 5 or 10 μm. Data are means of at least three biological replicates. Error bars in panel l represent SEMs.
1112 Two-tailed unpaired Student's t-test was performed for data in panels c,d, f and i. Chi-squared test
1113 was performed for data in panels k and l. In graphs, average values for each biological replicate are
1114 shown by colored dots (each color corresponds to a different biological replicate). * denotes p<0,05;
1115 **denotes p<0,01; *** denotes p< 0,005; **** denotes p<0,001. Source Data are provided as a
1116 Source Data file.
1117
1118 **Fig. 4: DDK and MiDAS act as surveillance mechanisms to limit genome instability**
1119 **accumulation in aneuploid cells. a**, Experimental workflow for the analysis of DNA damage and
1120 chromosome aberrations in G1 cells following DDK and MiDAS inhibition in the cell cycle after
1121 chromosome missegregation induction. **b,c,d,** Representative images (b) and quantification of
1122 FANCD2 (c) and γH2AX (d) accumulation in cytokinesis-blocked pseudo-G1 cells expressing LCK-
1123 GFP (for FANCD2: n=90 for Ctrl, n=72 for Ctrl+DDKi; n=84 for Ctrl+MiDASi, n=81 for
1124 Ctrl+DDKi+MiDASi; n=87 for Aneu, n=88 for Aneu+DDKi, n=90 for Aneu+MiDASi, n=86 for
1125 Aneu+DDKi+MiDASi. For γH2AX: n=90 for Ctrl, n=72 for Ctrl+DDKi; n=84 for Ctrl+MiDASi,
1126 n=81 for Ctrl+DDKi+MiDASi; n=88 for Aneu, n=93 for Aneu+DDKi, n=95 for Aneu+MiDASi,
1127 n=90 for Aneu+DDKi+MiDASi.). **e**, Representative mFISH images of G1 cell-derived metaphase-
1128 like chromosomes from aneuploid cells upon DDK and MiDAS inhibition. **f**, Zoomed image of the
1129 chromosome highlighted in the dotted-line box in panel e (image on the right) from the aneuploid
1130 sample in which DDK and MiDAS were inhibited showing a translocation between chromosome 19
1131 and chromosome 18. **g**, Quantification of the percentage of cells with more than 1 translocation in
1132 the two samples (n=18 for Aneu, n=19 for Aneu+DDKi+MiDASi). **h,i,j**, Representative images (h)
1133 and quantification of FANCD2 (i) and γH2AX (j) non-random distribution between the daughter
1134 pseudo-G1 cells (for FANCD2: n=86 for Ctrl, n=78 for Aneu. For γH2AX: n=90 for Ctrl, n=90 for
1135 Aneu). Cells treated with aphidicolin (RS, replication stress) were used as a positive control (n=46
1136 for FANCD2 and n=81 for γH2AX). Ctrl, control (DMSO pulsed). Aneu, aneuploid cells (Mps1
1137 inhibitor pulsed). RS, replication stress (aphidicolin treated cells). DDKi, DDK inhibitor. MiDASi,
1138 MiDAS inhibitor. NDD, non-random distribution. Scale bars, 5 or 10 μm. LUT was inverted for
1139 FANCD2 and γH2AX images. Blue borders in images are based on DAPI staining and define nuclei.
1140 Data are means of at least three biological replicates, except for data in panels e-g that were obtained
1141 from three biological replicates. Error bars in panels i and j represent SEMs. Two-tailed unpaired
1142 Student's t-test was performed for data in panels c and d. Fisher's test was performed for data in
1143 panels i and j. In graphs, average values for each biological replicate are shown by colored dots (each

1144 color corresponds to a different biological replicate). * denotes p<0,05; ** denotes p<0,01; ***
1145 denotes p< 0,005; **** denotes p<0,001. Source Data are provided as a Source Data file.
1146
1147 **Fig. 5: Aneuploid cells that retained their proliferative capacity exhibit reduced levels of DNA**
1148 **damage and genome instability. a**, Senescence-associated β-galactosidase staining in control and
1149 aneuploid cells. Doxorubicin-treated cells were used as a positive control. **b**, Experimental workflow
1150 for a method to separate and recover both cycling and arrested aneuploid cells based on FACS-sorting
1151 and the usage of a fluorescent substrate of the b-galactosidase enzyme. **c**, FACS profiles showing the
1152 percentage of DDAOG-positive cells in aneuploid cells incubated or not with the DDAOG substrate.
1153 **d**, Senescence-associated β-galactosidase staining in cycling and arrested aneuploid cells obtained
1154 after sorting. **e**, Cell cycle profiles of control, aneuploid, aneuploid cycling and aneuploid arrested
1155 FUCCI-cells analyzed by live-cell imaging. **f**, Quantification of percentage of G1 cells in the four
1156 samples analyzed by live-cell imaging (n=100 for each sample). **g,h,i,** Representative images (g) and
1157 quantification of FANCD2 (h) and γH2AX (i) foci per cell in the different samples. Only EdU
1158 negative cells were analyzed in order to exclude the contribution of S-phase cells present in the non-
1159 arrested cell samples (n=123 for Ctrl, n=123 for Aneu, n=123 for Aneu cyc, n=89 for Aneu arr). **j**,
1160 scWGS of cycling and arrested aneuploid cells. Single cells are represented in rows and chromosomes
1161 are plotted as columns (n=50 for Aneu cyc, n=53 for Aneu arr). Copy-number states are indicated in
1162 colors (see legend at the bottom). hTERT RPE-1 cells have clonal gains of 10q and chromosome 12[73].
1163 **k,** Quantification of cells with at least 3 aneuploid chromosomes in the two samples (n=50 for Aneu
1164 cyc, n=53 for Aneu arr). Gains of 10q and chromosome 12 were excluded from the analysis. Ctrl,
1165 control (DMSO pulsed). Aneu or An, aneuploid cells (Mps1 inhibitor pulsed). Aneu cycling or An
1166 cyc, aneuploid cycling cells. Aneu arrested or An arr, aneuploid arrested cells. Scale bars, 5μm. LUT
1167 was inverted for FANCD2 and γH2AX images. Blue borders in images are based on DAPI staining
1168 and define nuclei. Data are means of three biological replicates, except for panel f (one replicate) and
1169 k (two replicates). Error bars in panel e represent SDs. Two-tailed unpaired Student's t-test was
1170 performed for data in panels h and i. Fisher's test was performed for data in panel k. In graphs, average
1171 values for each biological replicate are shown by colored dots (each color corresponds to a different
1172 biological replicate). * denotes p<0,05; **** denotes p<0,001. Source Data are provided as a Source
1173 Data file.
1174
1175 **Fig. 6: Cycling aneuploid cells display decreased karyotype aberrations and upregulate DNA**
1176 **repair genes in comparison with arrested aneuploid cells. a**, Experimental workflow for the
1177 assessment of genome instability levels by live-cell imaging in aneuploid cycling cells expressing

1178 H2b-GFP. **b**, Representative images of cell divisions in the different samples. For illustration
1179 purposes, images were deconvoluted by using the Huygens software using the deconvolution express
1180 function. **c**, Quantification of mitotic errors in 3 cell division rounds in control (n=187) and aneuploid
1181 cycling (n=274) cells. Cells treated with the Mps1 inhibitor just before starting the time-lapse were
1182 used as a positive control for mitotic errors (n=83). **d**, Volcano plot illustrating the differentially
1183 expressed pathways between cycling and arrested aneuploid cells. Specific gene sets are highlighted
1184 in color. **e,** Heat-map showing the z-scores of single-sample GSEA (ssGSEA) scores for DNA
1185 damage-related gene sets. **f,g,** Quantification of γH2AX foci (f) and 53BP1 bodies (g) in cycling
1186 (n=150) and arrested aneuploid (n=150) cells upon IR exposure. Only EdU negative cells were
1187 analyzed in order to exclude the contribution of S-phase cells present in the non-arrested cell samples.
1188 **h,i,j,** Association between ssGSEA score for GOBP DNA repair (h) or GOBP DNA synthesis
1189 involved in DNA repair (i) or GOBP regulation of DNA repair (j) and proliferation capacity in top
1190 vs. bottom quartiles of cancer cell lines from[51]. Ctrl, control (DMSO pulsed). Aneu cycling or cyc,
1191 aneuploid cycling cells. Aneu arrested or arr, aneuploid arrested cells. M, mother division. D,
1192 daughter division. GD, grand-daughter division. Mps1i, Mps1 inhibitor. In panel e, #1 and #2 refer
1193 to biological replicates. Not irrad., not irradiated. Data are means of two biological replicates, except
1194 for data in panels f and g (three replicates). Error bars represent SEMs. Shaded error bands in panels
1195 f,g are shown above and below for arrested and cycling cells, respectively. Fisher's test was
1196 performed for data in panel c. Two-tailed paired t-test was performed for data in panels f and g. Two-
1197 tailed Mann-Whitney test was performed for data in panels h-j.In panel c, average values for each
1198 biological replicate are shown by colored dots (each color corresponds to a different biological
1199 replicate). **** denotes p<0,001. Source Data are provided as a Source Data file.
1200
1201 **Fig. 7: Final model.** A model for how aneuploidy induces genome instability and its consequences.
1202 See text for more details.
1203
1204 **Extended Data Fig. 1: Impact of thymidine block and reversine treatment on DNA damage**
1205 **accumulation. a**, Experimental setup for the FACS analysis of thymidine treated cells. **b**,
1206 Representative flow cytometry profiles of propidium-iodide stained cells. Gating strategy is
1207 illustrated on top. **c**, Experimental setup for the analysis of DNA damage upon thymidine block or
1208 doxorubicin treatment. **d,e**, Representative images (d) and relative quantification (e) of γH2AX foci
1209 per cell (n=150 for each sample). **f,g**, Representative images (f) and relative quantification (g) of
1210 γH2AX foci per cell (n=150 for each sample). **h,i,** Representative mFISH images of karyotypes
1211 obtained from the 1st (n=77) and the 2nd mitosis (n=101) in control cells (h) and relative quantification

1212 of percentage of cells with chromosome gains, losses or translocations (i). T(10,X) and +12 were
1213 excluded from the analysis as they are clonal in hTERT RPE-1 cells. Untr, untreated, Thy, thymidine.
1214 Mps1i, Mps1 inhibitor. W/O, washout. Doxo, doxorubicin. Ctrl, control (DMSO pulsed). Scale bars,
1215 5µm. LUT was inverted for γH2AX images. Blue borders in images are based on DAPI staining and
1216 define nuclei. Data are means of three biological replicates. Two-tailed unpaired Student's t-test was
1217 performed for data in panels e and g. In graphs, average values for each biological replicate are shown
1218 by colored dots (each color corresponds to a different biological replicate). **** denotes p <0,001.
1219 Source Data are provided as a Source Data file.
1220
1221 **Extended Data Fig. 2: Impact of mimosine treatment and Mps1 inhibition on cell cycle and**
1222 **DNA damage. a**, Experimental setup for the FACS analysis of mimosine treated cells. **b**,
1223 Representative flow cytometry profiles of propidium-iodide stained cells. **c**, Experimental setup for
1224 the analysis of DNA damage upon mimosine treatment. **d,e**, Representative images (d) and relative
1225 quantification (e) of γH2AX foci per cell (n=150 for each sample). **f**, Representative flow cytometry
1226 profiles of propidium-iodide stained cells treated with aphidicolin as in panel a. Untr, untreated.
1227 Mps1i, Mps1i inhibition. Mimo, mimosine. W/O, washout. Scale bars, 5µm. LUT was inverted for
1228 γH2AX images. Blue borders in images are based on DAPI staining and define nuclei. Data are means
1229 of three biological replicates. Two-tailed unpaired Student's t-test was performed for data in panel e,
1230 where average values for each biological replicate are shown by colored dots (each color corresponds
1231 to a different biological replicate). *** denotes p<0,005.
1232 **Extended Data Fig. 3: DDK inhibition leads to exacerbation of replication stress particularly in**
1233 **aneuploid cells. a,** Experimental workflow for the analysis of DNA replication stress markers in S-
1234 phase upon treatment with PP1 analog II, 1-NM-PP1, in hTERT RPE-1 cells expressing wild-type or
1235 analog-sensitive Cdc7. A short EdU pulse was performed before cell harvest in order to label S-phase
1236 cells. **b,** Western blot analysis of MCM2 and phoshoS40-MCM2 in cells expressing wt or as Cdc7.
1237 GAPDH was used as loading control. **c,d,** Representative images (c) and quantification (d) of
1238 FANCD2 foci per S-phase cell in control or aneuploid cells ± 1-NM-PP1 inhibitor in the two cell
1239 lines (n=153 for each sample). **e,f,** Representative images (e) and quantification (f) of RPA foci per
1240 S-phase cell in control or aneuploid cells ± 1-NM-PP1 inhibitor in the two cell lines (n=153 for each
1241 sample). **g,h,** Representative images (g) and quantification (h) of pChk1 foci per S-phase cell in
1242 control or aneuploid cells ± 1-NM-PP1 inhibitor in the two cell lines (n=156 for each sample). **i,**
1243 FACS profiles showing the percentage of live cells in control and aneuploid cells. Gating strategy is
1244 illustrated on the left. Cells treated with staurosporin for 24 hours were used as a positive control of
1245 cell death. Ctrl, control (DMSO pulsed). Aneu, aneuploid cells (Mps1 inhibitor pulsed). wt, wild-

1246 type. as, analog-sensitive. Scale bars, 5µm. LUT was inverted for FANCD2, RPA and pChk1 images.
1247 Blue borders in images are based on DAPI staining and define nuclei. Data are means of three
1248 biological replicates. Two-tailed unpaired Student's t-test was performed for data in panel e, where
1249 average values for each biological replicate are shown by colored dots (each color corresponds to a
1250 different biological replicate). * denotes p<0,05; *** denotes p< 0,005; **** denotes p<0,001. Source
1251 Data are provided as a Source Data file.
1252
1253 **Extended Data Fig. 4: Effect of RO3306 treatment on cell cycle and DNA damage. a**,
1254 Quantification of S-phase duration by live-cell imaging in control (n=125) and aneuploid (n=106)
1255 cells. The graph refers to the experiment in Figure 3, panels a-d. **b**, Quantification of mitotic division
1256 timing upon SAC inhibition in control (n=54 for Ctrl Normal M, n=12 for Ctrl Normal M + Mps1i,
1257 n=16 for Ctrl Abnormal M, n=48 for Ctrl Abnormal M + Mps1i) and aneuploid (n=35 for Aneu
1258 Normal M, n=7 for Aneu Normal M + Mps1i, n=47 for Aneu Abnormal M, n=53 for Aneu Abnormal
1259 M + Mps1i) cells that underwent normal or abnormal mitosis. **c**, Experimental setup for the FACS
1260 analysis of RO3306 treated cells. **d**, Representative flow cytometry profiles of propidium-iodide
1261 stained cells. **e**, Experimental setup for the analysis of DNA damage upon RO3306 treatment. **f,g**,
1262 Representative images (f) and relative quantification (g) of γH2AX foci per cell (n=150 for each
1263 sample). **h,i**, Representative images (h) and relative quantification (i) of telomeric EdU foci in control
1264 (n=111) and aneuploid (n=180) cells. Aphidicolin treated cells were used as positive control of
1265 replication stress (n=367). For illustration purposes, images were processed using Fiji. Briefly,
1266 images were filtered with median filter and background was subtracted using the dedicated Fiji
1267 function. Ctrl, control (DMSO pulsed). Aneu, aneuploid cells (Mps1 inhibitor pulsed). Mps1i, Mps1
1268 inhibitor. W/O, washout. Scale bars, 5µm. LUT was inverted for γH2AX images. Blue borders in
1269 images are based on DAPI staining and define nuclei. Data are means of at least three biological
1270 replicates, except for data in panel b (two replicates). Two-tailed unpaired Student's t-test was
1271 performed for data in panels a, b and g. Chi-squared test was performed for data in panel i. In graphs,
1272 average values for each biological replicate are shown by colored dots (each color corresponds to a
1273 different biological replicate). *** denotes p< 0,005; **** denotes p<0,001. Source Data are provided
1274 as a Source Data file.
1275
1276 **Extended Data Fig. 5: POLD3 depletion and consequent MiDAS inhibition result in a further**
1277 **increase in aneuploid cell genome instability. a,** Experimental workflow for the assessment of
1278 MiDAS occurrence in prometaphase cells and genome instability in the following G1 phase upon
1279 siRNA-mediated POLD3 depletion in hTERT RPE-1 cells. **b,** Western blot analysis of POLD3 in

1280 cells transfected with siRNA scramble or against POLD3. Vinculin was used as loading control. **c,d**,
1281 Representative images (c) and quantification (d) of EdU foci in prometaphase cells in control and
1282 aneuploid cells (n=150 for each sample). Cells treated with aphidicolin (RS, replication stress) were
1283 used as a positive control (n=150). **e-g,** Representative images (e) and quantification of 53BP1 body
1284 (f) and micronucleus (g) accumulation in control and aneuploid G1 cells upon POLD3 depletion
1285 (n=195 for each sample). Cells treated with aphidicolin (RS, replication stress) were used as a positive
1286 control (n=195). Ctrl, control (DMSO pulsed). Aneu, aneuploid cells (Mps1 inhibitor pulsed). RS,
1287 replication stress (aphidicolin treated cells). siScramble, transfected with non-targeting siRNA.
1288 siPOLD3, transfected with siRNA against POLD3. Scale bars, 5 µm. Data are means of three
1289 biological replicates. Error bars represent SEMs. Two-tailed unpaired Student's t-test was performed
1290 for data in panel d. Chi-squared or Fisher's test was performed for data in panels f and g. In graphs,
1291 average values for each biological replicate are shown by colored dots (each color corresponds to a
1292 different biological replicate). * denotes p<0,05; **denotes p<0,01; **** denotes p<0,001. Source
1293 Data are provided as a Source Data file.
1294
1295 **Extended Data Fig. 6: RNF168 asymmetric partitioning between daughter cells occurs at higher**
1296 **frequency in cells with reduced proliferative capacity. a,** Experimental workflow for the analysis
1297 of RNF168 distribution during cell division by live-cell imaging using hTERT RPE-1 cells expressing
1298 PCNA-chromobodies, RNF168-miRFP and H2b-GFP. **b,c**, Representative images of symmetric (b)
1299 and asymmetric (c) distribution of RNF168 between daughter cells. For presentation purposes,
1300 images were processed using Fiji. Briefly, images were filtered with gaussian blur, background was
1301 subtracted using the dedicated Fiji function and gamma transformation was applied to enhance the
1302 RNF168-miRFP signal. **d**, Quantification of RNF168 non-random distribution between daughter G1
1303 cells in control (n=288) and aneuploid (n=459 for REV, n=250 for AZ3146) cells. **e**, Quantification
1304 of cell divisions with DNA damage transmission in aneuploid cells (treated with reversine) that had
1305 divided less than 4 times ('Low', n=103) or at least 4 times ('High', n=286) over the almost 120 hour-
1306 time lapse experiment. **f**, Quantification of cell divisions with asymmetric distribution of DNA
1307 damage in aneuploid cells (treated with reversine) that had divided less than 4 times ('Low', n=103)
1308 or at least 4 times ('High', n=286) over the almost 120 hour-time lapse experiment. Ctrl, control
1309 (DMSO pulsed). Aneu, aneuploid cells (Mps1 inhibitor pulsed). White borders in images are based
1310 on H2b-GFP signal and define nuclei. Data are means of three biological replicates. Error bars
1311 represent SEMs. Chi-squared or Fisher's test was performed for data in panel d. Two-tailed unpaired
1312 Student's t-test was performed for data in panels e and f. In graphs, average values for each biological

1313 replicate are shown by colored dots (each color corresponds to a different biological replicate). **
1314 denotes p<0,01; **** denotes p<0,001. Source Data are provided as a Source Data file.
1315
1316 **Extended Data Fig. 7: Separation and characterization of aneuploid cycling and arrested cells.**
1317 **a**, Senescence-associated β-galactosidase staining in control and aneuploid cells at different time
1318 points after the Mps1 inhibitor pulse (n=127 for Ctrl 24h, n=102 for Ctrl 48h, n=117 for Ctrl 72h,
1319 n=160 for Aneu 24h, n=160 for Aneu 48h, n=116 for Aneu 72h). Doxorubicin-treated cells were used
1320 as a positive control (n=250 for Ctrl, n=128 for Doxo). **b,c,** FACS profiles showing the percentage of
1321 DDAOG positive cells in DMSO (b) and doxorubicin (c) treated cells, used as a positive control.
1322 Gating strategy is illustrated on the left of panel c. **d,** Illustration depicting the change in nuclear color
1323 in the FUCCI cells. **e**, Representative images showing the starting (0h) and end point (24h) of the
1324 time-lapse in the four different samples (n=100 for each sample). **f,g** Histogram showing the
1325 percentage of cycling (n=50) or arrested (n=53) aneuploid cells with a given gained or lost
1326 chromosome. The graph refers to the experiment in Figure 5 j,k. Ctrl, control (DMSO pulsed). Aneu,
1327 aneuploid cells (Mps1 inhibitor pulsed). Aneu cycling, aneuploid cycling cells. Aneu arrested,
1328 aneuploid arrested cells. Doxo, doxorubicin. Scale bar, 20μm. In graphs, average values for each
1329 biological replicate are shown by colored dots (each color corresponds to a different biological
1330 replicate). Source Data are provided as a Source Data file.
1331
1332 **Extended Data Fig. 8: Kinetics of DNA damage repair in aneuploid cells and respective controls**
1333 **upon IR exposure. a-f** Representative images (a,b) and quantification of γH2AX (c,e) and 53BP1
1334 bodies (d,f) per cell (n=150 for each sample in all data sets). Only EdU negative cells were analyzed
1335 in order to exclude the contribution of S-phase cells present in the non-arrested cell samples. **g,h**,
1336 Gene set enrichment analysis (GSEA) plots showing enrichment of p53 and DNA damage repair
1337 pathways in aneuploid cycling vs control cells. Ctrl, control (DMSO pulsed). Aneu, aneuploid cells
1338 (Mps1 inhibitor pulsed). Aneu cycling, aneuploid cycling cells. Aneu arrested, aneuploid arrested
1339 cells. Not irrad., not irradiated. LUT was inverted for γH2AX and 53BP1 images. Blue borders in
1340 images are based on DAPI staining and define nuclei. Data are means of three biological replicates.
1341 Shaded error bands in panels c-f represent SEMs. Source Data are provided as a Source Data file.
1342
1343 **Extended Data Table 1: List of genes differentially expressed in arrested vs. cycling aneuploid**
1344 **cells.** Data were obtained by RNAseq (Fig. 6).
1345
1346

1347

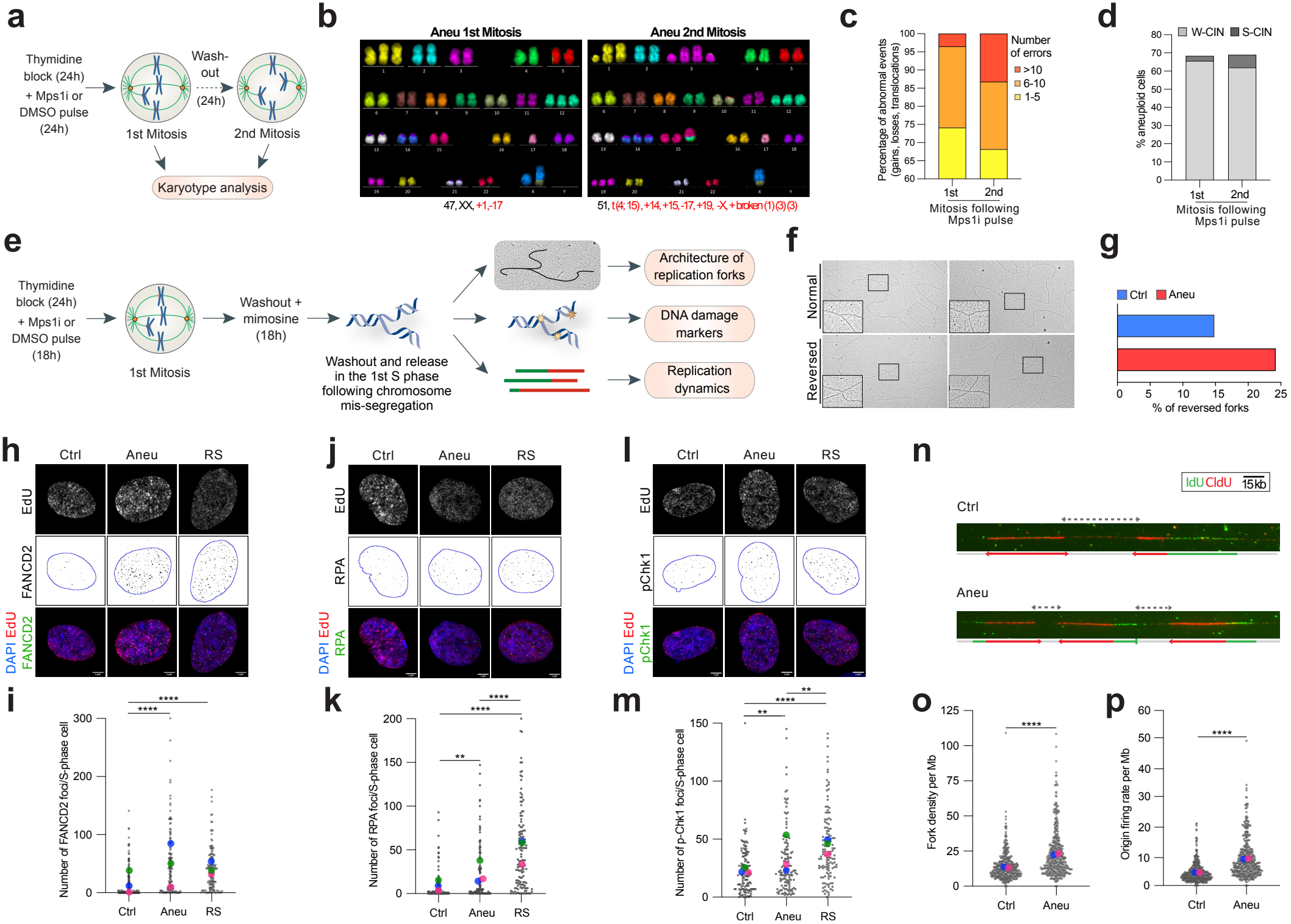
a
Thymidine block (24h) + Mps1i or DMSO pulse (24h)
Wash-out (24h)
1st Mitosis
2nd Mitosis
Karyotype analysis
b
Aneu 1st Mitosis
Aneu 2nd Mitosis
47, XX, +1,-17
51, t(4;15),+14,+15,-17,+19, -X,+broken(1)(3)(3)
c
Percentage of abnormal events (gains, losses, translocations)
Number of errors
>10
6-10
1-5
1st
2nd
Mitosis following Mps1i pulse
d
W-CIN
S-CIN
% aneuploid cells
1st
2nd
Mitosis following Mps1i pulse
e
Thymidine block (24h) + Mps1i or DMSO pulse (18h)
1st Mitosis
Washout + mimosine (18h)
Washout and release in the 1st S phase following chromosome mis-segregation
Architecture of replication forks
DNA damage markers
Replication dynamics
f
Normal
Reversed
g
Ctrl
Aneu
% of reversed forks
h
Ctrl
Aneu
RS
EdU
FANCD2
DAPI EdU FANCD2
j
Ctrl
Aneu
RS
EdU
RPA
DAPI EdU RPA
l
Ctrl
Aneu
RS
EdU
pChk1
DAPI EdU pChk1
n
IdU CldU
15kb
Ctrl
Aneu
i
Number of FANCD2 foci/S-phase cell
Ctrl
Aneu
RS
k
Number of RPA foci/S-phase cell
Ctrl
Aneu
RS
m
Number of p-Chk1 foci/S-phase cell
Ctrl
Aneu
RS
o
Fork density per Mb
Ctrl
Aneu
p
Origin firing rate per Mb
Ctrl
Aneu

Figure 1

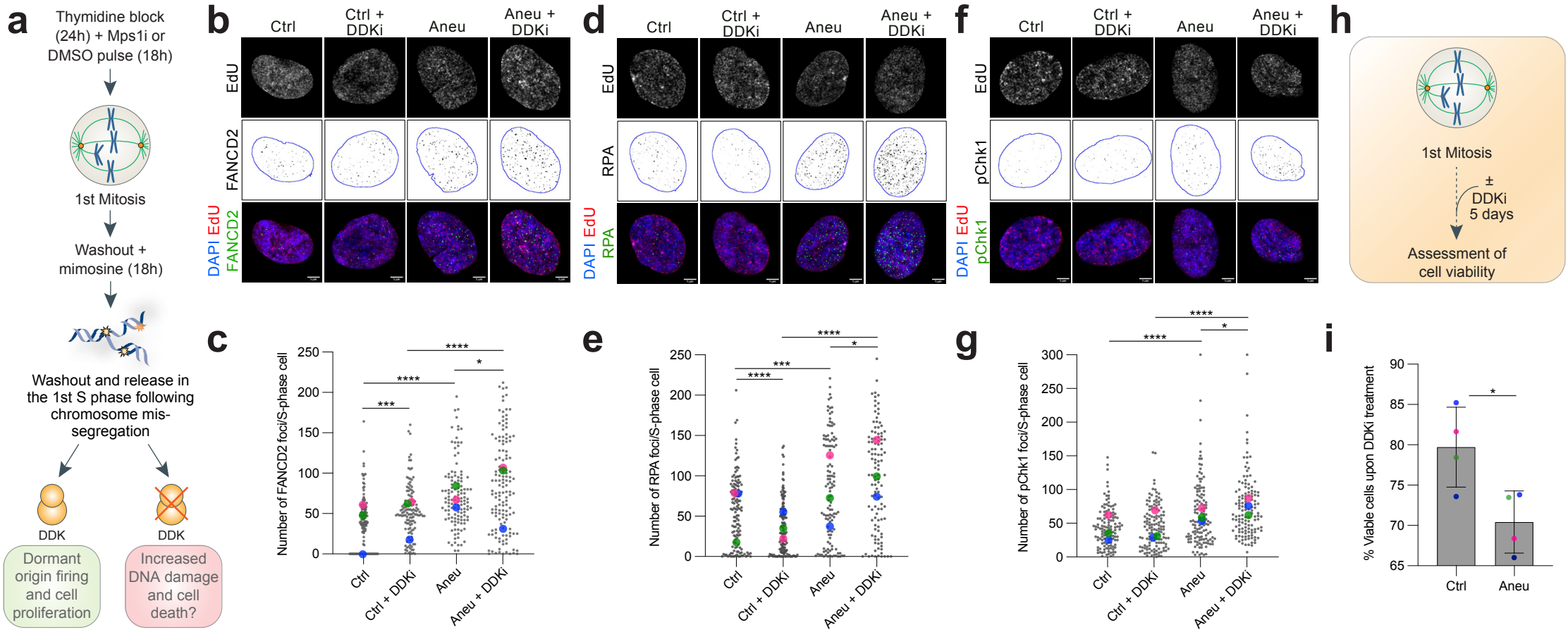
a
Thymidine block (24h) + Mps1i or DMSO pulse (18h)
1st Mitosis
Washout + mimosine (18h)
Washout and release in the 1st S phase following chromosome mis-segregation
DDK
DDK
Dormant origin firing and cell proliferation
Increased DNA damage and cell death?
b
Ctrl
Ctrl + DDKi
Aneu
Aneu + DDKi
EdU
FANCD2
DAPI EdU FANCD2
d
RPA
DAPI EdU RPA
f
pChk1
DAPI EdU pChk1
h
1st Mitosis
± DDKi 5 days
Assessment of cell viability
c
Number of FANCD2 foci/S-phase cell
e
Number of RPA foci/S-phase cell
g
Number of pChk1 foci/S-phase cell
i
% Viable cells upon DDKi treatment
Ctrl
Ctrl + DDKi
Aneu
Aneu + DDKi

Figure 2

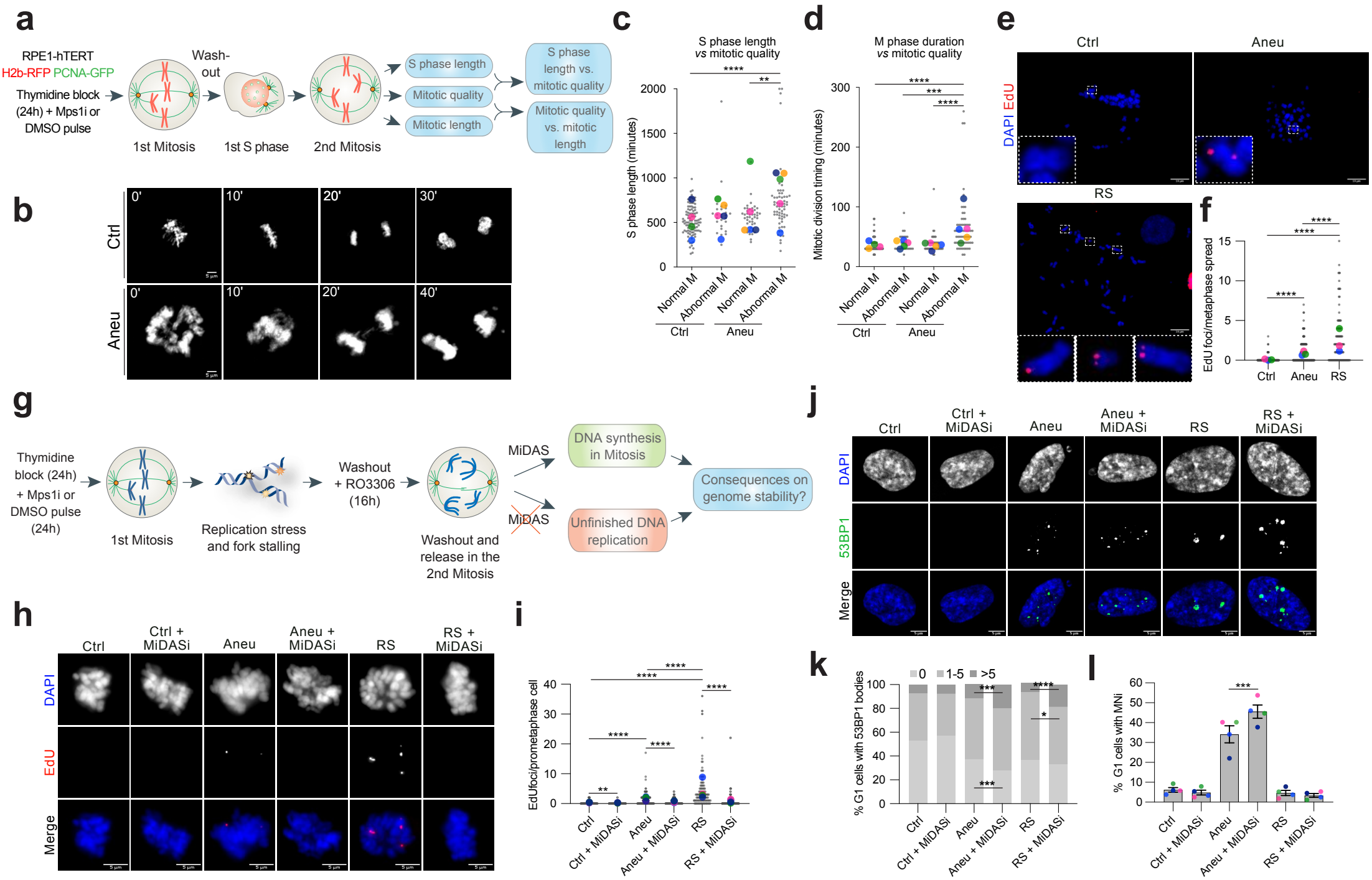
a
RPE1-hTERT
H2b-RFP PCNA-GFP
Thymidine block (24h) + Mps1i or DMSO pulse
Wash-out
1st Mitosis
1st S phase
2nd Mitosis
S phase length
Mitotic quality
Mitotic length
S phase length vs. mitotic quality
Mitotic quality vs. mitotic length
b
Ctrl
Aneu
0'
10'
20'
30'
40'
c
S phase length vs mitotic quality
S phase length (minutes)
Normal M
Abnormal M
Ctrl
Aneu
d
M phase duration vs mitotic quality
Mitotic division timing (minutes)
e
Ctrl
Aneu
RS
DAPI EdU
f
EdU foci/metaphase spread
g
Thymidine block (24h) + Mps1i or DMSO pulse (24h)
1st Mitosis
Replication stress and fork stalling
Washout + RO3306 (16h)
Washout and release in the 2nd Mitosis
MiDAS
DNA synthesis in Mitosis
Unfinished DNA replication
Consequences on genome stability?
h
Ctrl
Ctrl + MiDASi
Aneu
Aneu + MiDASi
RS
RS + MiDASi
DAPI
EdU
Merge
i
EdUfoci/prometaphase cell
j
53BP1
k
% G1 cells with 53BP1 bodies
0
1-5
>5
l
% G1 cells with MNi

Figure 3

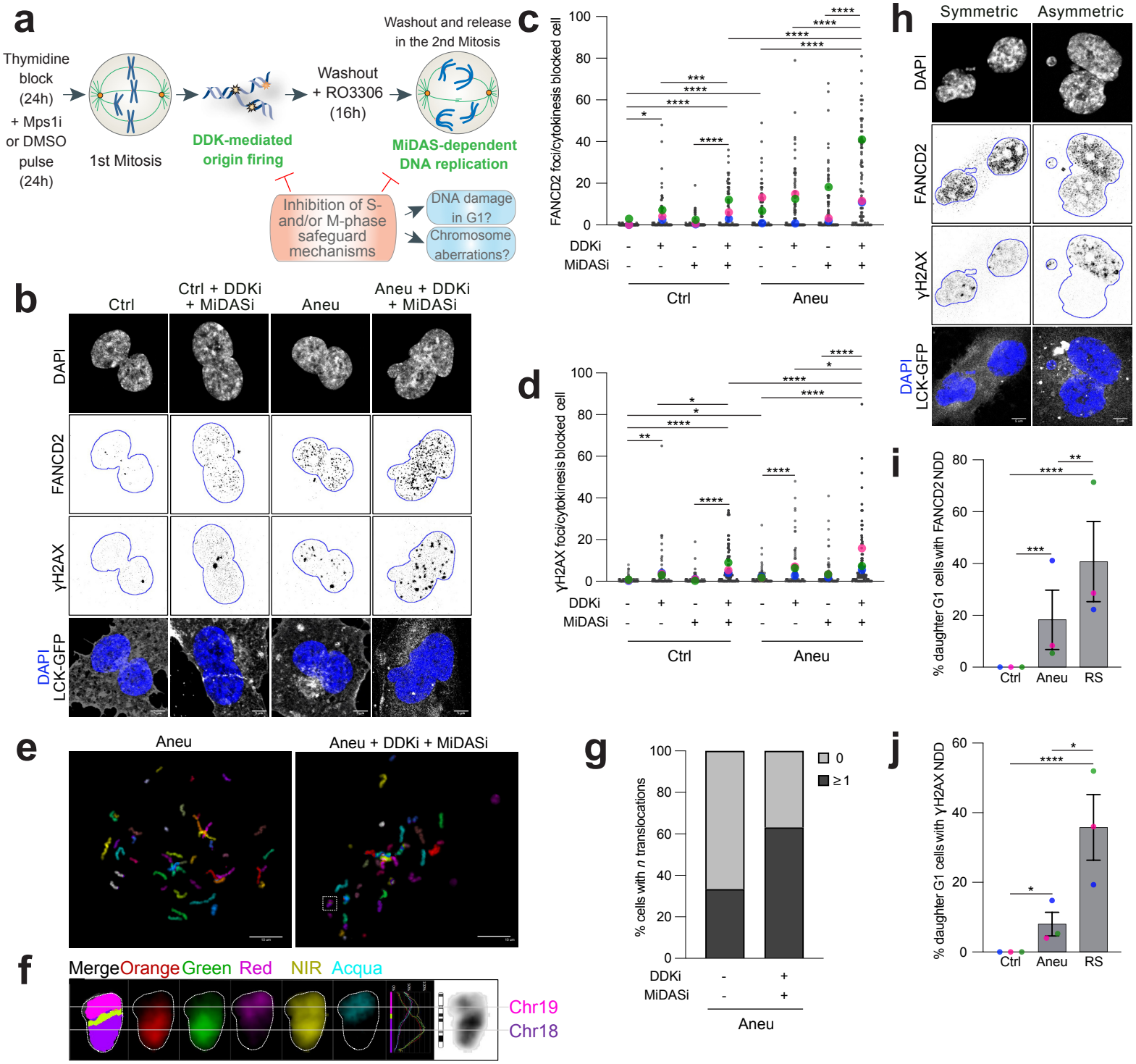
a
Thymidine block (24h) + Mps1i or DMSO pulse (24h)
1st Mitosis
DDK-mediated origin firing
Washout + RO3306 (16h)
Washout and release in the 2nd Mitosis
MiDAS-dependent DNA replication
Inhibition of S- and/or M-phase safeguard mechanisms
DNA damage in G1?
Chromosome aberrations?
b
Ctrl
Ctrl + DDKi + MiDASi
Aneu
Aneu + DDKi + MiDASi
DAPI
FANCD2
γH2AX
DAPI LCK-GFP
c
FANCD2 foci/cytokinesis blocked cell
DDKi
MiDASi
Ctrl
Aneu
d
γH2AX foci/cytokinesis blocked cell
DDKi
MiDASi
Ctrl
Aneu
e
Aneu
Aneu + DDKi + MiDASi
f
Merge Orange Green Red NIR Acqua
Chr19
Chr18
g
% cells with n translocations
0
≥1
DDKi
MiDASi
Aneu
h
Symmetric
Asymmetric
DAPI
FANCD2
γH2AX
DAPI LCK-GFP
i
% daughter G1 cells with FANCD2 NDD
Ctrl
Aneu
RS
j
% daughter G1 cells with γH2AX NDD
Ctrl
Aneu
RS

Figure 4

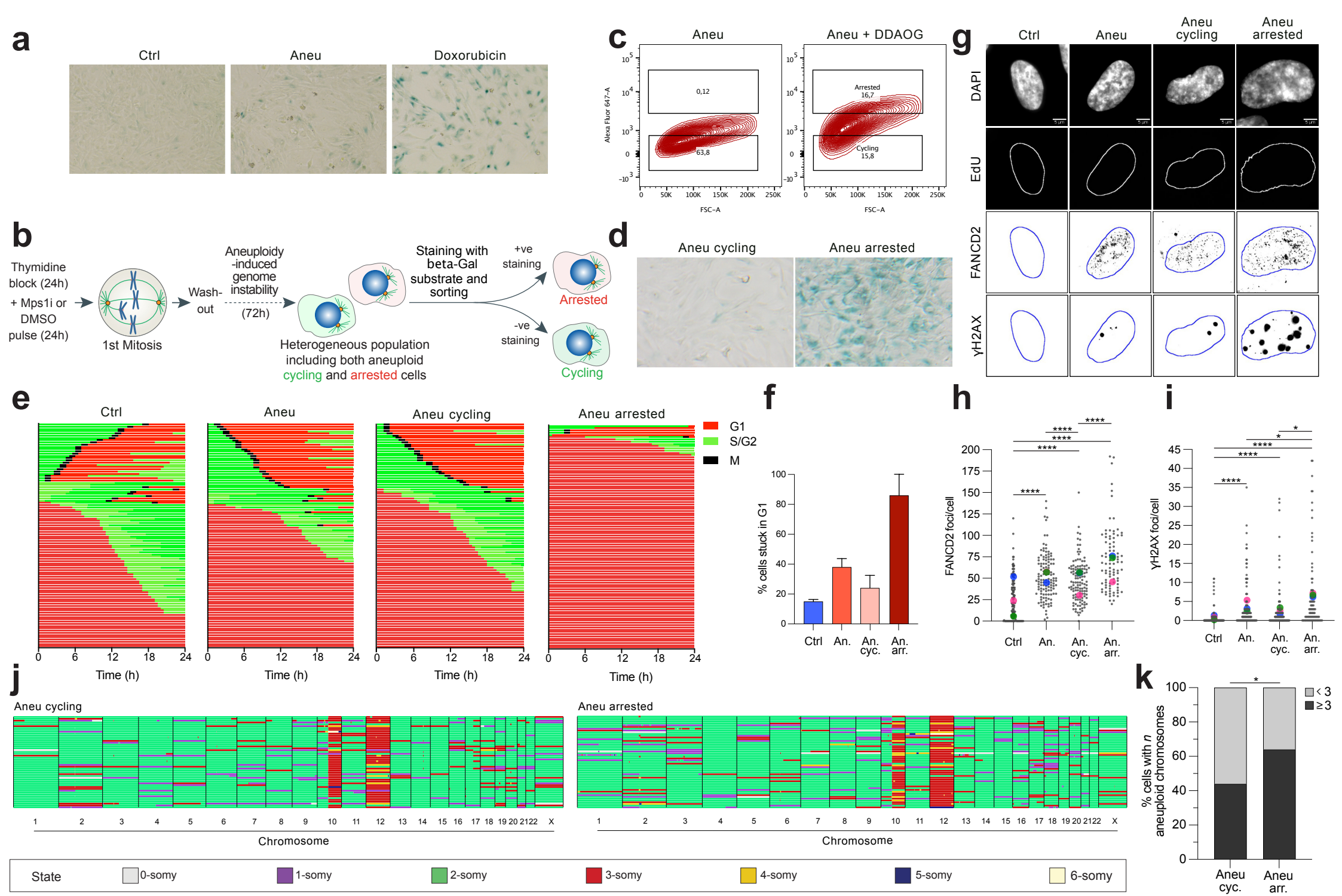
a
Ctrl
Aneu
Doxorubicin
b
Thymidine block (24h) + Mps1i or DMSO pulse (24h)
1st Mitosis
Wash-out
Aneuploidy -induced genome instability
(72h)
Heterogeneous population including both aneuploid cycling and arrested cells
Staining with beta-Gal substrate and sorting
+ve staining
-ve staining
Arrested
Cycling
c
Aneu
Aneu + DDAOG
Alexa Fluor 647-A
FSC-A
0,12
63,8
Arrested 16,7
Cycling 15,8
d
Aneu cycling
Aneu arrested
e
Ctrl
Aneu
Aneu cycling
Aneu arrested
G1
S/G2
M
Time (h)
f
% cells stuck in G1
Ctrl
An.
An. cyc.
An. arr.
g
Ctrl
Aneu
Aneu cycling
Aneu arrested
DAPI
EdU
FANCD2
γH2AX
h
FANCD2 foci/cell
i
γH2AX foci/cell
j
Aneu cycling
Aneu arrested
Chromosome
State
0-somy
1-somy
2-somy
3-somy
4-somy
5-somy
6-somy
k
% cells with n aneuploid chromosomes
< 3
≥ 3
Aneu cyc.
Aneu arr.

Figure 5

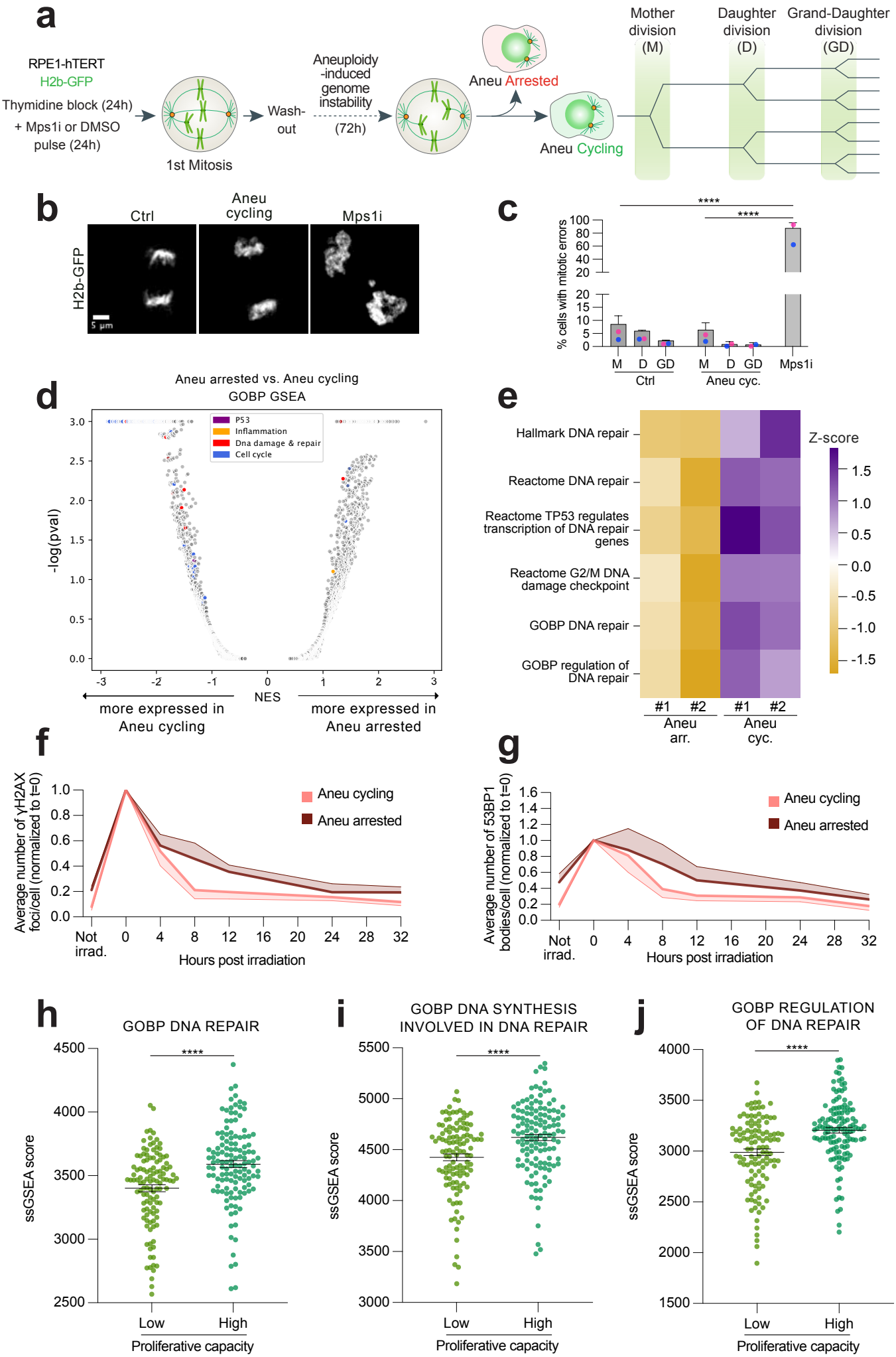
a
RPE1-hTERT
H2b-GFP
Thymidine block (24h)
+ Mps1i or DMSO
pulse (24h)
1st Mitosis
Wash-out
Aneuploidy -induced genome instability
(72h)
Aneu Arrested
Aneu Cycling
Mother division (M)
Daughter division (D)
Grand-Daughter division (GD)
b
Ctrl
Aneu cycling
Mps1i
H2b-GFP
5 µm
c
% cells with mitotic errors
M D GD M D GD Mps1i
Ctrl
Aneu cyc.
d
Aneu arrested vs. Aneu cycling
GOBP GSEA
P53
Inflammation
Dna damage & repair
Cell cycle
-log(pval)
NES
more expressed in Aneu cycling
more expressed in Aneu arrested
e
Hallmark DNA repair
Reactome DNA repair
Reactome TP53 regulates transcription of DNA repair genes
Reactome G2/M DNA damage checkpoint
GOBP DNA repair
GOBP regulation of DNA repair
Z-score
#1 #2 #1 #2
Aneu arr.
Aneu cyc.
f
Average number of γH2AX foci/cell (normalized to t=0)
Aneu cycling
Aneu arrested
Not irrad.
Hours post irradiation
g
Average number of 53BP1 bodies/cell (normalized to t=0)
Aneu cycling
Aneu arrested
Not irrad.
Hours post irradiation
h
GOBP DNA REPAIR
ssGSEA score
Low High
Proliferative capacity
i
GOBP DNA SYNTHESIS INVOLVED IN DNA REPAIR
ssGSEA score
Low High
Proliferative capacity
j
GOBP REGULATION OF DNA REPAIR
ssGSEA score
Low High
Proliferative capacity

Figure 6

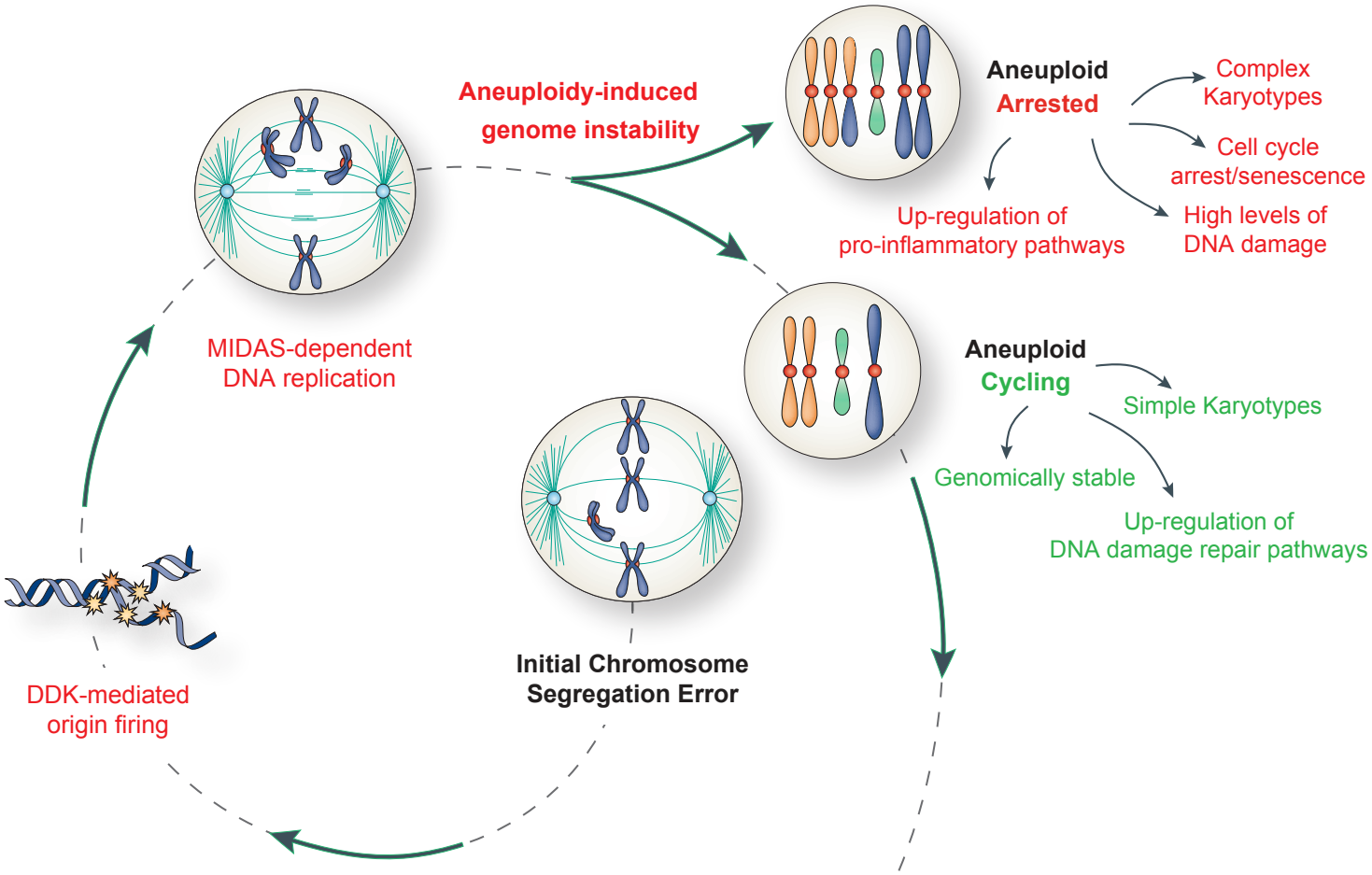
Aneuploidy-induced
genome instability
Aneuploid
Arrested
Complex
Karyotypes
Cell cycle
arrest/senescence
High levels of
DNA damage
Up-regulation of
pro-inflammatory pathways
MIDAS-dependent
DNA replication
Aneuploid
Cycling
Simple Karyotypes
Genomically stable
Up-regulation of
DNA damage repair pathways
Initial Chromosome
Segregation Error
DDK-mediated
origin firing

Figure 7